remote sensing

MDPI

Article

Feasibility Study on Measuring Atmospheric CO_2 in Urban Areas Using Spaceborne CO_2-IPDA LIDAR

Ge Han [1], Hao Xu [2,*], Wei Gong [2,*], Jiqiao Liu [3], Juan Du [3], Xin Ma [4] and Ailin Liang [5]

1 School of Remote Sensing and Information Engineering, Wuhan University, Wuhan 430079, China; udhan@whu.edu.cn
2 State Key Laboratory of Information Engineering in Surveying, Mapping and Remote Sensing, Wuhan University, Wuhan 430079, China
3 Key Laboratory of Space Laser Communication and Detection Technology, Shanghai Institute of Fine Mechanics and Optics, Chinese Academy of Sciences, Shanghai 201800, China; liujiqiao@siom.ac.cn (J.L.); dujuan2014@siom.ac.cn (J.D.)
4 Electronic Information School, Wuhan University, Wuhan 430079, China; maxinwhu@whu.edu.cn
5 School of Remote Sensing and Surveying Engineering, Nanjing University of Information Science and Technology, Pukou District, Ningliu Road 219, Nanjing 210044, China; ireneliang@whu.edu.cn
* Correspondence: xiaohao190081@whu.edu.cn (H.X.); weigongwhu@gmail.com (W.G.); Tel.: +86-181-6400-0242 (H.X.); +86-180-8668-2787 (W.G.)

Received: 4 May 2018; Accepted: 19 June 2018; Published: 21 June 2018

Abstract: Since over 70% of carbon emissions are from urban areas, it is of great importance to develop an effective measurement technique that can accurately monitor atmospheric CO_2 in global urban areas. Remote sensing could be an effective way to achieve this goal. However, due to high aerosol loading in urban areas, there are large, inadequately resolved areas in the CO_2 products acquired by passive remote sensing. China is planning to launch the Atmospheric Environment Monitoring Satellite (AEMS) equipped with a CO_2-light detecting and ranging (LIDAR) system. This work conducted a feasibility study on obtaining city-scale column CO_2 volume mixing ratios (XCO_2) using the LIDAR measurements. A performance framework consisting of a sensor model, sampling model, and environmental model was proposed to fulfill our demand. We found that both the coverage and the accuracy of the LIDAR-derived city-scale XCO_2 values were highly dependent on the orbit height. With an orbit height of 450 km, random errors of less than 0.3% are expected for all four metropolitan areas tested in this work. However, random errors of less than 0.3% were obtained in only two metropolitan areas with an orbit height of 705 km. Our simulations also showed that off-nadir sampling would improve the performance of a CO_2-Integrated Path Differential Absorption (IPDA) LIDAR system operating in a 705 km orbit. These results indicate that an active remote sensing mission could help to effectively measure XCO_2 values in urban areas. More detailed studies are needed to reveal the potential of such equipment for improving the verification of carbon emissions and the estimation of urban carbon fluxes.

Keywords: atmospheric measurements; LIDAR (light detecting and ranging); CO_2; error analysis; IPDA (Integrated Path Differential Absorption)

1. Introduction

Accurate measurements of the atmospheric column dry-air mixing ratios of CO_2 (abbreviated as XCO_2 hereafter) not only help to understand the feedback mechanisms of carbon cycle processes related to climate change, simulating future scenarios that can be used to accurately formulate scientific countermeasures [1], but also help to estimate carbon emission levels, supporting the establishment of a carbon emissions trading market [2]. More than 70% of the world's CO_2 emissions are from

urban areas [3]. It is of great significance to clarify the city-scale carbon fluxes or carbon emissions to understand the impact of human activities on the carbon cycle [4–6], laying a foundation for customized carbon reduction plans. Therefore, the development of an atmospheric XCO_2 monitoring system for urban areas is a task with great scientific and application value.

Current XCO_2 monitoring systems can be classified into two categories, namely, in situ and remote sensing measurements. Generally, synergistic fusions of in situ and remote sensing observations allow significantly useful information to be obtained regarding carbon fluxes or emissions. The in situ measurements can provide highly accurate results, but the spatial coverage is insufficient to constrain the inversions of the carbon fluxes with a high spatial resolution due to the limited number and uneven distribution of the stations [7–10]. Theoretically, one can deploy a large number of in situ observation stations to obtain very detailed information on the carbon fluxes of urban areas or point emissions. However, such a plan would definitely yield vast costs that are unaffordable within the current technology levels. In addition, column XCO_2 measurements are less sensitive than surface point CO_2 measurements to the redistribution of emitted CO_2 by small-scale processes and, thus, may allow for more precise emission trend detections from urban regions [11]. Compared with the in situ measurements, satellite-based sensors can obtain XCO_2 values over larger areas at a relatively lower cost. Thus, it is a more feasible method for monitoring atmospheric CO_2 concentrations in urban areas globally. The existing satellite-based CO_2 sensors are mainly based on passive remote sensing techniques that have already improved the estimation of large-scale carbon fluxes to some extent [12]. However, the accuracy of the XCO_2 products derived from passive remote sensing are seriously affected by aerosols [13–16]. Atmospheric pollution in urban areas is more serious than in other areas. The high concentration of the aerosol optical depth (AOD) is considered as a detrimental factor for obtaining accurate XCO_2 values from space-based passive sensors [17]. Retrievals of XCO_2 values are excluded for further analysis when the AOD was higher than 0.3 for passive remote sensing systems, such as the Orbiting Carbon Observatory-2 (OCO-2) satellite [18]. Moreover, due to the limitations of the solar elevation angle, passive remote sensing systems would fail to obtain useful observations in high latitudes, where many important metropolitan areas are located [19].

The integrated-path differential absorption (IPDA) light detecting and ranging (LIDAR) system that relies on laser signals reflected from hard targets has a better signal-to-noise ratio (SNR) than range-resolved differential absorption LIDAR and passive remote sensing techniques and is recognized as the most promising next-generation CO_2 sensing technology [20]. IPDA LIDAR belongs to the active remote sensing techniques that are immune to the solar elevation issue and, thus, could provide global coverage. Additionally, differential processes helps reduce the effect of aerosols significantly and enables reliable measurements in regions with high AODs [21]. Groups from the United States and the Europe Union have competed to develop prototypes of a CO_2-IPDA LIDAR system over the past decade and have carried out a number of airborne experiments [22–30]. It the meantime, Japanese groups have also developed a CO_2-IPDA LIDAR system [31,32]. China is now interested in developing its own CO_2-IPDA LIDAR system that will be onboard on the Atmospheric Environment Monitoring Satellite (AEMS) due to be launched between 2021–2025 according to the Medium and Long-Term Development Planning of the National Civil Space Infrastructure. At the beginning, the requirement on the random error of monthly XCO_2 product acquired by the CO_2-IPDA equipped on AEMS is below 0.3% with spatial resolutions of 50 km and 100 km over lands and oceans, respectively. Our previous study has already suggested that such a requirement can be fulfilled in most areas in China and its surroundings [33]. It is worth noting that the requirement on measurements of XCO_2 using remote sensing was defined as 2.5 ppm (~0.7%@360 ppm) on a $8^\circ \times 10^\circ$ footprint in 2001 [7]. In the assessment report for the Advanced Space Carbon and Climate Observation of Planet Earth (A-SCOPE) satellite the requirement was redefined as 1.5 ppm (~0.4%@380 ppm) with a horizontal resolution of 50 km in 2008 [34]. It is worth noting that all those requirements are derived from the scientific goal that scientists want to constrain the fluxes to within 0.02 Pg C yr^{-1} on a scale of 1000 km $\times$ 1000 km.

Regarding estimations of urban carbon emissions using space-based remotely sensed XCO_2 measurements, Hakkarainen found that there was a positive relationship between the OCO-2-derived XCO_2 values and emission intensities, though such a relationship cannot be expressed by a quantitative mathematical model [35]. In that study, a median filter was used to extract XCO_2 anomalies related with carbon emissions. Kiemle and Amediek argued that it is possible to retrieve the emission rate of the strong point sources using space-based IPDA-LIDAR-derived XCO_2 values and meteorological data [26,36]. In their frameworks, Gaussian shapes were used to simulate exhaust plumes from the point sources. On that basis, the emission rate was retrieved using wind speed and wind direction. Menzies has already demonstrated the ability of an airborne IPDA laser absorption spectrometer to retrieve the emission rate of a point source by using a simple box model [30]. Additionally, the atmospheric inversion technique was widely used to estimate carbon fluxes on a continental scale [37,38]. More endeavors are urgently required to develop appropriate frameworks for estimating carbon emissions rates or fluxes at the urban scale. However, before this, it is of great significance to determine the accuracy and the precision of XCO_2 data obtained from urban areas.

Inspiring by the above studies, we try to figure out whether China's planning ASEM is adequate to obtain useful XCO_2 data in urban areas, thus laying a foundation for further estimation of anthropogenic carbon emission or city-scale carbon fluxes. We believe that two scientific goals would pose different requirements on XCO_2 products in terms of accuracy, precision, and resolution/coverage. To estimate the emission of anthropogenic carbon point emission, the accuracy of single observation of XCO_2 and the availability of instantaneous meteorological data with respect to the satellite transit time would be of great significance. To the opposite, the precision of XCO_2 in a certain area would be more important than the accuracy when one tried to estimate city-scale carbon fluxes by using CO_2 horizontal gradients. It is worth noting that no universal method for estimating the anthropogenic carbon point emission or city-scale carbon fluxes by using satellite-based remotely-sensed data has been established. Therefore, there are no specific requirements on accuracy, precision, and resolution with respect to CO_2 measuring in urban using satellite remote sensing means. In this work, we have to use requirements defined for estimation of carbon fluxes on continental scale as a reference. Consequently, we focus on what performance ASEM-CO_2-IPDA can obtain, but not whether the mission can achieve some specific scientific goals in this work.

Several performance modeling studies of a spaceborne greenhouse-gas-IPDA LIDAR system have been performed in the past decade [33,39–41]. However, the cloud coverage issues have never been integrated into the performance models. Though the potential of a spaceborne CO_2-IPDA to retrieve XCO_2 above dense clouds has been demonstrated using airborne measurements [42,43], XCO_2 in the lower troposphere is the critical parameter required to indicate human-induced carbon emission in urban areas. Hence, we took the effect of clouds into consideration in this work in order to achieve better modeling results. Additionally, the orbit sampling pattern was also introduced into the performance modeling frameworks instead of using simple sample point averages in terms of the study areas.

Hence, we will show a dedicated study aimed at analyzing the performance of China's space-based CO_2-IPDA LIDAR system quantitatively in four representative metropolitan areas of China to determine whether accurate XCO_2 measurements can be obtained in urban areas. Unlike the passive remote sensing of CO_2 that can scan perpendicular to the direction of the satellite orbit, IPDA, in practice, has sensors that only operate in point mode due to the unaffordable power consumption and cost of implementing a scan mode. Consequently, there would be some inevitable areas where the LIDAR would never receive signals. The sampling pattern thus plays a very important role in determining the accuracy of the city-scale XCO_2 measurements. It is critical to pay attention to the number of cloud-free observations. A significant advantage of this study over other similar research [33,40,41,44] is that the cloud product was included in the simulations to study its effect on shot averaging. It is worth noting that LIDAR can also work with dense cloud coverage [43]. Therefore, concentrations of CO_2 from the top of the cloud to the top of the atmosphere can be

retrieved using the reflected signals from dense clouds. Nonetheless, CO_2 molecules within the atmospheric boundary layer are our first priority for XCO_2 measurements in urban areas because they are the direct indicator of human activities. Consequently, only the cloud-free pseudo-observations were regarded as useful data in this work.

The following sections are organized as follows: the frameworks for estimating the performance of the city-scale XCO_2 measurements are introduced in Section 2. Also present in that section are the relevant study area backgrounds and material information. In Section 3, we present the results of the simulations and discuss which factor is the dominant factor related to the performance of the CO_2-IDPA LIDAR system for measuring city-scale XCO_2 in urban areas. In Section 4, we present further discussions on potential improvements to the AEMS design. Finally, we summarize our findings in Section 5.

2. Materials and Methods

Performance evaluation of a CO_2-IPDA LIDAR includes three parts, the random error, the systemic error, and the coverage. The random error is the index for indicating the precision, while the systematic error is the index for indicating the accuracy. The concept of "coverage" for a LIDAR is quite different from that for a passive sensor because observations of a LIDAR are discrete distributed points, but not images. Consequently, we constructed a sampling model to simulate observations. Finally, the random error is of major importance to this work because it is more geographically variable.

Figure 1 shows the frameworks we used herein to estimate random errors of city-scale XCO_2 by using China's CO_2-IPDA LIDAR in urban areas. It is worth noting the direct physical quantity of an IPDA LIDAR is the number density of a target gas. However, the carbon cycle community conventionally uses the dry-air mixing ratio to describe the concentration of CO_2. Therefore, it is necessary to transform the concentration unit in number density into in mixing ratio by using an estimation of the number density of the air. Such a procedure depends on accurate measurements or estimations of atmospheric profiles of temperature, pressure, and humidity. Now, we are not sure about which meteorological products would be used by China's IPDA LIDAR in the future. Accuracies of meteorological products in urban areas would be higher than those in other areas because there are meteorological stations in urban areas. Given that the uncertainties of temperature and pressure are 0.5 k and 0.5 hPa, respectively, the error derived from unit transformation would be no more than 0.1%.

The performance evaluation considers the interactive relationship among the sensor model, environmental model, and sampling model. Hence, all three models are involved in this work. Parameters of the sensor are defined according to the configuration of China's planning CO_2-IPDA LIDAR. Parameters of the environmental model are derived from remotely-sensed data. In this section, we show the methodologies used to simulate random and orbit samplings, as well as the values of relevant parameters used in simulations.

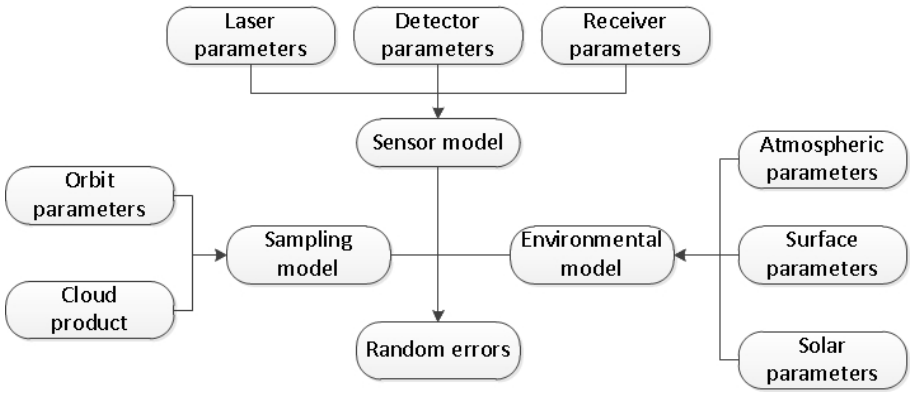

Figure 1. Frameworks for estimation of random errors of CO_2-IPDA in urban areas.

2.1. Introduction to the Instrumentation

China is planning to launch the AEMS during 2021–2025 to realize simultaneous observations of $PM_{2.5}$ and CO_2. The administration of this mission would be Ministry of Environmental Protection, China. China Aerospace Science and Technology Corporation takes charge of developing this satellite. Shanghai Institute of Optics and Fine Mechanics takes charge of developing the CO_2-IPDA LIDAR. Onboard there will be both passive and active sensors. Except for the CO_2-IPDA LIDAR, other sensors include a Mie-LIDAR, a wide imaging spectrometer, a multi-angle polarization imager, and a polarization scanner. As the core mission of this satellite is to retrieve $PM_{2.5}$ with a high accuracy, there have to be some compromises for the CO_2-IPDA LIDAR. The transit time should be set at noon to obtain strong solar radiance reflected from the Earth's surface, which is beneficial to obtain observations with higher signal-noise-ratio for the passive sensors. However, the solar radiance is regarded as a noise source for LIDAR sensors. Moreover, the most appropriate transit time for a CO_2-IPDA LIDAR would be dawn and dusk when characteristics of respiration and photosynthesis effects might be observed. The other factor is the orbit height. Several IPDA LIDAR sensors, such as MERLIN (Methane Remote Sensing LIDAR Mission) and ASCENDS (Active Sensing of CO2 Emissions over Nights, Days, and Seasons), are planned to be sent to the orbit height of ~450 km. However, the orbit height of the AEMS is 705 km, which could be an obstacle to highly accurate measurements of XCO_2 [33]. To our knowledge, such a design has no advantage in terms of CO_2 measuring compared with the configuration of ASCENDS or A-SCOPE. However, a higher height orbit would result in a longer service time, providing more opportunity to study the relationship between atmospheric pollution and greenhouse gases. The designed configuration of that sensor and detailed information on its main laser can be found in other works. Hence, we skip those parts in the main body of this work. Readers can also find them in Appendix A.

2.2. Study Area

Four metropolitan areas in China are selected as the study area of this work, namely Beijing, Shanghai, Guangzhou, and Wuhan. They are located in Northern, Eastern, Southern, and Central China, respectively. Since they are not geographically adjacent, samples of the satellite would not be similar in the four metropolitan areas. Additionally, the climatic characteristics of these metropolitan areas are quite different from each other. Hence, their cloud fraction and AOD would also be evidently different. Figure 2 shows the locations of those metropolitan areas.

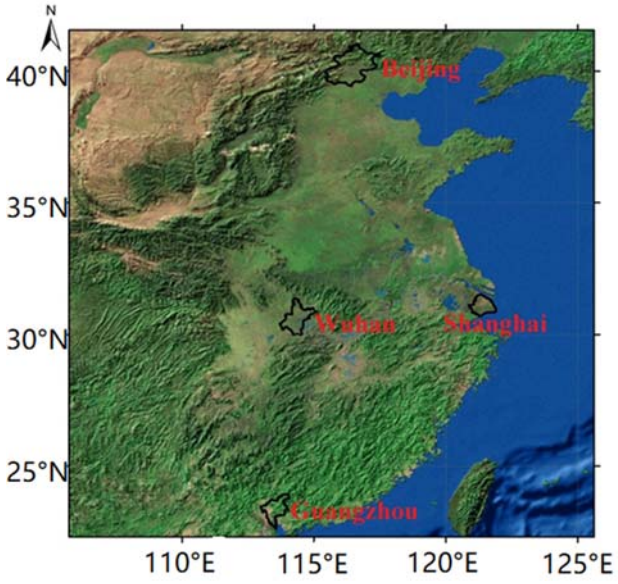

Figure 2. Locations of the four megalopolises.

2.3. Random Errors

The random error of XCO_2 measurements consists of two parts. One is from estimation of the number density of the air and the other is from the estimation of the number density of the CO_2. The latter part is equivalent to that of optical depth due to the differential absorption effects of CO_2, expressed as follows [39]:

$$\frac{\Delta\delta_{CO2}}{\delta_{CO2}} = \frac{1}{2\delta_{CO2}}\sqrt{\frac{1}{n_{shots}}\left(\frac{1}{SNR_{on}^2}+\frac{1}{SNR_{off}^2}+\frac{1}{(SNR_{on}^L)^2}+\frac{1}{\left(SNR_{off}^L\right)^2}\right)} \quad (1)$$

where δ_{CO2} is the optical depth due to absorption of CO_2, $\Delta\delta_{CO2}$ is the standard deviation of δ_{CO2}, n_{shots} denotes the number of statistically independent pulse pairs, $SNR_{on,off}^L$ represents the statistical fluctuation of laser pulse energy measurements, and $SNR_{on,off}$ is the mean SNR of the LIDAR returns. It is also worth noting that speckle noise should also be included in Equation (1), theoretically. However, through our preliminary simulations we found the speckle SNR is at least three orders of magnitude higher than $SNR_{on,off}$. Therefore, we ignore errors derived from speckle noises in this work.

In this work, n_{shots} is determined by orbit sampling and cloud fraction. An orbit sampling model will be used to simulate distribution of nadir dots. Then we used the vector file of four megalopolises to intersect with nadir dots. Finally, the cloud fraction is used to reduce the selected nadir dots and then we obtained n_{shots}. Only two dominant error sources, namely the dark current noise and the solar background noise, are considered herein for simplification. A detailed calculation method of SNR can be found in Appendix B.

2.4. Systematic Errors

In this work, sources of systemic error are divided into four categories, namely, atmosphere, line parameters, transmitter, and satellite. The error derived from the linewidth, a transmitter-related parameter, can be corrected via a gas absorption cell which is a common component of the frequency stabilization unit [12]. Hence, linewidth error will not be included in this work. The uncertainties of relevant parameters are shown in Table 1. The information is provided by Ministry of Environmental Protection, China.

Auxiliary data are essential to derive geophysical data product (XCO_2) from raw measurement data (LIDAR echoes). Meteorological forecasting centers like the European Centre for Medium-range Weather Forecasting would be able to provide such data. For the ongoing AEMS, China Meteorological Administration would assume the task of providing auxiliary data. Table 2 shows uncertainties of temperature and pressure would be just 0.5 K and 0.5 hPa, respectively, which are lower than those used in Ingmann's report [34]. However, Ehret had also assumed uncertainties of temperature and pressure as 0.5 K and 0.5 hPa respectively [39]. To our knowledge, such assumptions on uncertainties of temperature and pressure are beyond the ability of current assimilation models. However, the AEMS will not be launched before 2021. Hence, the assumption is reasonable given the evolution of meteorological data assimilation models.

Spectroscopic parameters used in our simulations are according to Predoi-Cross's work [45]. Hence, uncertainties of pressure broadening and temperature scaling exponents are according to that work. However, the uncertainties of line strength and pressure shift are not provided. In our work, we set uncertainties of the line strength and pressure shift in the light of HITRAN 2012 [46].

Regarding parameters of the laser and satellite platform, the frequency drift is assumed as 0.6 MHz, which is an extremely stringent requirement, while the spectral purity seems to be insufficient (in the later part we will discuss on this issue). The requirement on ranging ability is very stringent according to Table 2. Du et.al have demonstrated a ranging accuracy of ~1.5 m by using their CO_2-IPDA LIDAR prototype in 2017 [47], indicating that the assumption of this Table 1 on ranging accuracy is realistic.

Table 1. Parameters used to calculate the systematic errors.

Category	Name	Uncertainty
Atmospheric effect	Temperature	0.5 K
	Pressure	0.5 hPa
	Humidity	10%
Line parameter	Line strength	2%
	Pressure shift	1%
	Pressure broadening	0.08%
	Temperature scaling exponent	0.72%
Laser	Frequency drift	0.6 MHz
	spectral purity	99.9% + 0.45 nm
Satellite	Doppler shift along track	140 µrad
	Doppler shift across track	1000 µrad
	Misalignment of footprint	25 µrad
	Ranging accuracy	2 m

Referring to Singh's work [48], ε_s^i, the systematic error due to a specific factor F_i, can be expressed as:

$$\varepsilon_s^i = \frac{\left|\Delta\delta_{CO2}(F_i) - \overline{\Delta\delta_{CO2}}(F_i + \delta F_i)\right|}{\Delta\delta_{CO2}(F_i)}. \quad (2)$$

δF_i is the uncertainty of F_i. With a given value of F_i, we calculated $\Delta\delta_{CO2}$. $\overline{\Delta\delta_{CO2}}(F_i + \delta F_i)$ was obtained by randomly generating a set of numbers that follow a normal distribution defined by an average of 0 and a standard deviation equal to δF_i. F_i includes temperature, pressure, humidity, line strength, pressure shift, pressure broadening, and temperature scaling exponent, frequency drift, and spectral purity. Finally, the total systematic error would be the geometric addition of all specific errors.

Regarding the systematic error due to Doppler shifts, we first calculated the Doppler shifts by using Equation (3):

$$\Delta\nu = \frac{v\nu_0 sin\theta}{c} \quad (3)$$

where v is the speed along the track, ν_0 is the on-line frequency which can be transformed from the on-line wavenumber, θ is the angle between ground normal and the track direction, which should be 90°, theoretically. An uncertainty, $\delta\theta$, will be added to θ to calculate the Doppler shifts. Finally, we calculate Doppler shift-induced error by using Equation (3). It is worth noting that Doppler shifts can be classified into along-track and cross-track shifts. For the along-track Doppler shift, v is the speed of the satellite. For the cross-track Doppler shift, v is the wind speed.

The systematic error due to misalignment of footprint is related with the homogeneity of surface reflectance. Such an error can be determined only if we had surface reflectance products with a very high spatial resolution (<10 m). Amediek et al. indicated that the systematic error due to misalignment of footprint would not exceed 0.11% for the configuration of A-SCOPE [49].

Additionally, the systematic error due to atmospheric turbulences would be ignored in this work because the time interval between successive beams of different wavelength would be 200 µs, which could be seen as a frozen time for atmospheric activities.

Finally, the ranging accuracy will determines the accuracy of estimation of the surface pressure, thus exerts influences on retrieving XCO_2. However, according to a report from the European Space Agency, a ranging accuracy better than 3 m would permit the full neglecting of such an error to the overall error budget [34]. Consequently, the systematic error derived from ranging will be excluded.

It is worth noting that in Section 3.3, we focus on some primary error sources of the systematic error. However, it is not meant that we ignore other error sources. In the end, we would show a total the systematic error in which all error sources in Table 1 are included.

2.5. Orbit Sampling

Orbit sampling parameters can be calculated by using Equations (4)–(10), and are defined in Table 2, where t_0 is the time at which the satellite passes the ascending node. The geographical coordinates (latitude δ, longitude α) of nadirs of a satellite at a specific time t can be modeled by Equations (4) and (5). α_0 is the longitude of nadirs at t_0. we set it as 0° in this work. n is the angular velocity of satellite which is calculated by using Kepler's equation. $T_{satellite}$ is the orbit period which is calculated by using Kepler's Third Law. We can conclude from these equations that distribution patterns of nadirs of the satellite would be determined once the altitude of the satellite and the orbit inclination were given. However, the exact coordinates of nadirs would be solved only if α_0 and t_0 were known. Now, we still have no information on α_0 and t_0. Therefore, geographical coordinates of nadirs shown in the following simulations would not be exactly the same with real circumstances, whereas simulated distribution patterns would be of great significance to indicate the coverage of the planned satellite mission.

$$\delta = \arcsin(-\sin n\Delta t \cdot \sin t). \tag{4}$$

$$\alpha = \alpha_0 + \Delta\alpha. \tag{5}$$

$$\Delta\alpha = \arctan((-\sin\omega\Delta t \cdot \cos\Delta t + \cos\omega\Delta t \cdot \sin n\Delta t \cdot \cos i)/(\cos\omega\Delta t \cdot \cos n\Delta t + \sin\omega\Delta t \cdot \sin n\Delta t \cdot \cos i)). \tag{6}$$

$$n = \frac{\sqrt{\mu}}{a^{1.5}} \tag{7}$$

$$\Delta t = t - t_0. \tag{8}$$

$$T_{satellite} = \sqrt{4\pi^2 a^3/\mu} \tag{9}$$

$$a = 6371 + H_{satellite.} \tag{10}$$

Table 2. Orbit parameters.

Abbr.	Description/Value	Unit
δ	The latitude	degree
α	The longitude	degree
n	The angular velocity of satellite	rad/s
t	Any given time	s
t_0	The time at which the satellite passes the ascending node	s
Δα	The differential longitude between the ascending node and the current nadir	degree
ω	The angular velocity of earth/7.29×10^{-5}	rad/s
i	The orbit inclination/98.2	degree
μ	The geocentric gravitational constant/3.986×10^{14}	m^3/s^2
a	The semi-major axis of satellite orbit	km
Hsatellite	The altitude of satellite/705 or 450 in this work	km
Tsatellite	The orbit period	s

According to the laser parameters, the repetition frequency is 20 Hz. Hence, $\Delta t_n - \Delta t_{n-1}$ should be 0.05 s and there would be over 50 million samples in a month, globally, which is overwhelming for subsequent visualization. Consequently, the sample density was downscaled to 1% of the original density in the along-track direction for faster visualization, but kept 100% for the estimation of random errors.

2.6. Study Materials

In this study, AOD values in the study region were downloaded from the NASA Land and Atmospheres Archive and Distribution System (LAADS). Data from both Terra and Aqua were used. Data span the period from November 2015 to October 2016, and are at a 3-km spatial resolution. With this data, we calculated the yearly average for each pixel. Although there are numerous blank values in daily results, the resultant averaged values cover a region including all of China, except the Taklimakan Desert in the northwest region of the country. AOD is a season-related parameter.

However, we found that the number of useful daily AOD in urban areas is insufficient to derive a statistically significant average in many months.

Surface reflectance over land areas was obtained using MODIS (Terra + Aqua) 5-km, 16-d composite BRDF-adjusted data from band 6 (1.64 μm) and band 7 (2.13 μm). The synthetic surface reflectance for 1.57 μm was obtained by $Q_{1.57\,\mu m} = 0.727 \times Q_{1.64\,\mu m} + 0.309 \times Q_{2.13\,\mu m}$ [50]. The root mean square error of the synthetic surface reflectance is 1% according to Disney's work [50].

The model fit i. In each month, we collected three results on the 5th, 15th, and 25th, respectively, because the temporal variation of the surface reflectance is not dramatic. Then, the yearly product was obtained by averaging the monthly results. There are no blank values in our study area.

The cloud product was also obtained from MODIS MYD08_M3, which contains monthly 1 × 1 degree grid average values of cloud optical and physical properties. The cloud fractions from day and night are both included because IPDA can also work at night.

Image registration among reflectance, AOD and cloud fraction products were also conducted to generate spatially and temporally consistent input datasets for further analysis.

3. Results

3.1. Sample Point Distributions

As described previously, IPDA LIDAR cannot provide a scan or operate in image mode at present. When we try to use the data products to estimate city-scale carbon emissions or fluxes it is important to determine whether there are enough observations to provide the spatial coverage required for the calculations. Figure 3 shows the distribution of sample points with orbit heights of 450 and 705 km, respectively. The spatial coverage in Figure 4 is the same as in Figure 5. Along with other passive sensors, China's CO_2-IPDA LIDAR instrument has been designed to be onboard the AEMS. As a compromise between several sensors, the orbit height is at present planned as 705 km. The Active Sensing of CO_2 Emissions over Nights, Days, and Seasons (ASCENDS) satellite program has an orbital parameter height of 450 km. Given that the default AOD is 0.3 and the default reflectance is 0.2, the relative random error of each observation pair would be 2.1%. Hence, we need at least 5 and 49 observation pairs to achieve a random error of less than 1% and 0.3%, respectively. Taking the cloud cover into consideration, the necessary observation pairs would be further amplified five-fold, on average. Moreover, considering that the mean AOD in Chinese urban areas is evidently higher than 0.3, the necessary observation pairs would thus again need to amplified at least two-fold. Consequently, random errors of less than 0.3% would be expected only in those areas with at least five dots in Figures 3–5.

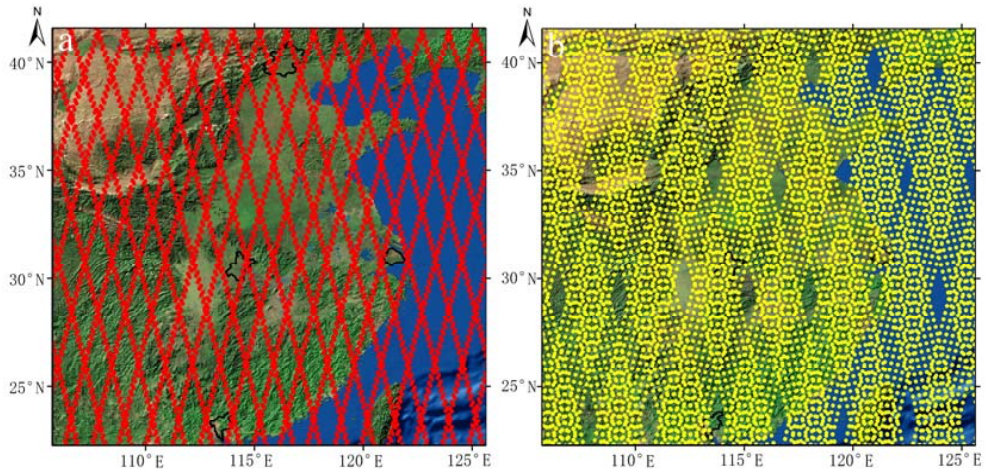

Figure 3. General monthly distribution of the nadir sample points. (**a**) Simulations with an orbit height of 705 km and (**b**) simulations with an orbit height of 450 km. For a better visualization, the sample points have already been downscaled to 1% along the track direction.

For each of the two orbit heights, both revisit periods are shorter than one month. Hence, the distribution pattern shown in Figure 3 would not be different even if the accumulation time were to be longer. After downscaling, globally, there are over 1,036,600 sample points for the two orbit heights. However, the distribution patterns between the two orbit heights are quite different. Figure 6a shows that sample points acquired from an orbit height of 705 km are more sparsely distributed than samples acquired from the 450 km orbit. This is due to the shorter revisit period of the 705 km orbit height.

Figure 4b,d show that sample points in both Beijing and Shanghai are distributed evenly when the orbit height is 450 km. Consequently, the resultant city-average XCO_2 measurements would be more representative and would not be vulnerable to carbon emissions located along the sample track. Moreover, compared to the 705 km orbit height, there are more sample points located within the boundary of both metropolitan areas when the orbit height is 450 km, resulting in a larger n_{shot} and, eventually, a smaller random error. Figure 6c shows that there are no sample points in Shanghai when the orbit height is 705 km. Shanghai has an area of 6340 km^2. In terms of area, there are many cities in China and in the world smaller than Shanghai. Consequently, we believe that an orbit height of 705 km would lead to insufficient and blank observations in many cities globally. It is worth noting that a design with an appropriate t_0 would obtain enough observations for a specific city, e.g., Shanghai. However, as a result, some other cities could then become blank and insufficiently covered areas. Consequently, if the orbit height was set to 705 km, we recommend that some critical cities should be selected as priorities and then an appropriate t_0 set so that most of the selected priority cities could obtain observations.

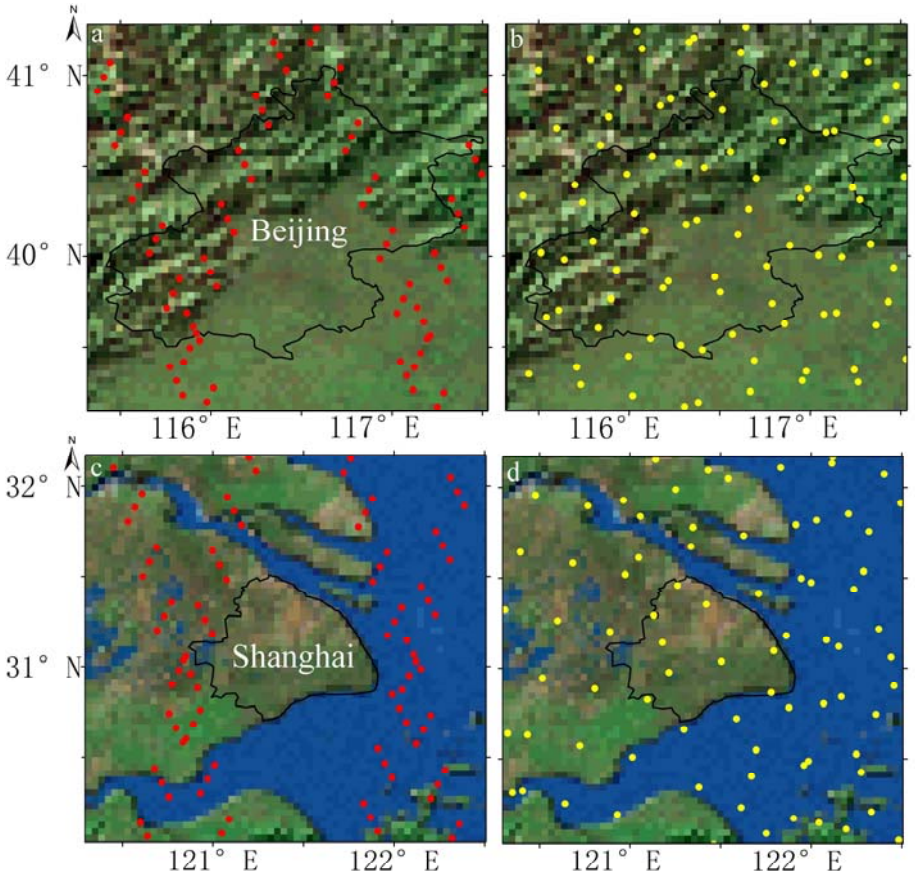

Figure 4. Sample points within the two orbit heights for Beijing and Shanghai. Red dots denote the 705 km height and yellow is for 450 km. (**a**,**b**) show the sample points in Beijing for the 705 and 450 km heights, respectively, while (**c**,**d**) show the sample points in Shanghai for the 705 and 450 km heights, respectively.

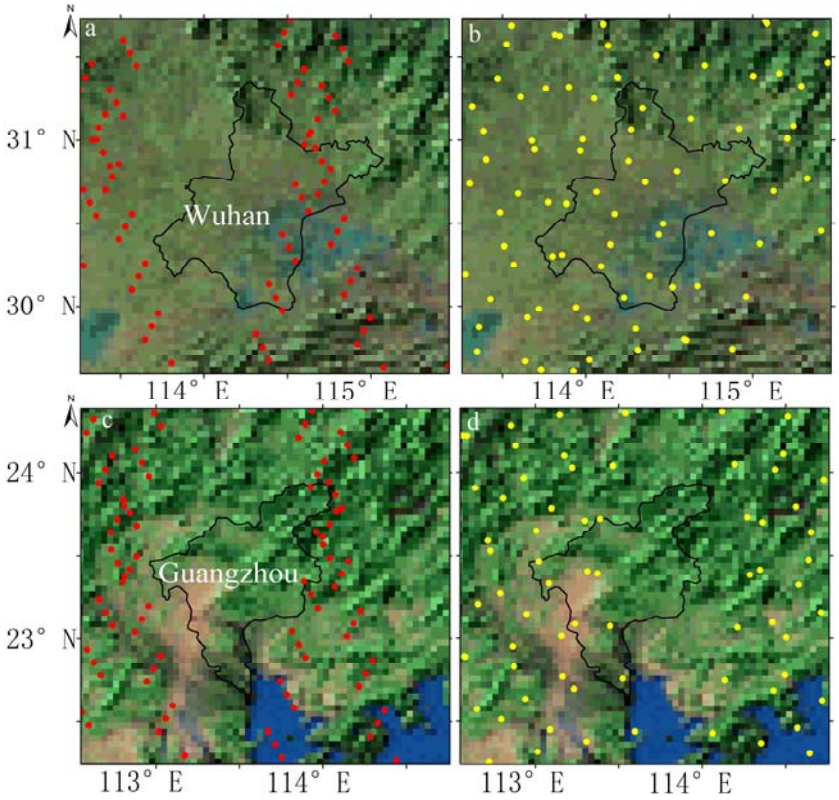

Figure 5. Sample points for the two orbit heights in Wuhan and Guangzhou. Red dots denote the 705 km height and yellow is for 450 km. (**a**,**b**) show the sample points in Wuhan for the 705 and 450 km heights, respectively, while (**c**,**d**) show the sample points in Guangzhou for the 705 and 450 km heights, respectively.

Figure 5a,b show that the number of 705 km sample points within Wuhan is roughly equal to that of 450 km sample points. However, the sample points for the 705 km orbit are located in the northeast of Wuhan, a suburban area. The built-up area of Wuhan is located in the center of the metropolis. Similar with Beijing, we do not think that the resultant city-average XCO_2 for Wuhan would be representative when the orbit height is 705 km and t_0 is 0. Figure 5c shows that there is inadequate sample point coverage in Guangzhou, representing a very similar condition to Shanghai. Figure 5d shows that there are also blank areas without coverage when the orbit height is 450 km. However, there are still some sample points in Guangzhou. We believe that there would be some "unlucky" cities where there would be no sample points, or very few with limited coverage when the orbit height is 450 km. However, in most cities, adequate sample points would be obtained when the orbit height is 450 km.

3.2. Estimation of the Random Error

Before determining the random error, we needed to calculate the environmental parameter statistics according to the schematic diagram shown in Figure 1. Regarding the solar radiance, our previous study demonstrated that even 10 times the normal value of 50 $mW \cdot m^{-2} \cdot nm^{-1} \cdot sr^{-1}$ would cause a negligible change in the random error (less than 0.02%). Consequently, solar radiance is not the dominant factor in determining the random error. In this simulation, we set the solar radiance as a constant value, 10 $mW \cdot m^{-2} \cdot nm^{-1} \cdot sr^{-1}$, two times of the normal value. Other parameters were processed as follows: After registration of the cloud, aerosol, and reflectance products, a temporal and spatially consistent dataset was obtained. Then, we extracted values from that dataset by intersecting with the nadir points of the CO_2-IPDA LIDAR. Finally, we calculated the statistics of the

extracted values in the form of vector files for four metropolitan areas. The results, shown in Table 3, were subsequently input into our random error estimation model (Equation (1)).

Table 3 shows that there are evident differences in the AOD among the four metropolitan areas. Shanghai ranks first in terms of the annual AOD, while Beijing ranks last. In 2015, the annual particulate matter with diameters of less than 2.5 μm ($PM_{2.5}$) mass concentrations were around 34, 66, 54, and 80 $\mu g \cdot m^{-3}$ for Guangzhou, Wuhan, Shanghai, and Beijing, respectively, according to data published by the China National Environmental Monitoring Center (http://106.37.208.233:20035/). Beijing is the most air-polluted city among the four study areas. We think two reasons could be responsible for the contradiction the AOD: $PM_{2.5}$ values and the air-pollution rankings. Firstly, Shanghai is the only coastal city among the four cities. The relative humidity of Shanghai is higher than that of Beijing and Wuhan. A higher humidity would lead to a stronger extinction coefficient and eventually lead to a higher AOD [51–53]. Guangzhou is located in Southern China which has a South Asian tropical monsoon climate. The humidity in Guangzhou is even higher than in Shanghai. However, the better air quality in Guangzhou results in a relatively lower AOD. Secondly, the inversion algorithm of the Moderate Resolution Imaging Spectroradiometer (MODIS) AOD product is designed to exclude observations obtained in high AOD conditions. Beijing suffers frequently from heavy air pollution during autumn and winter [54]. On these days, no AOD data would be available. The particular meteorological characteristics of Beijing determine that its air quality can either be very good, or very poor. The intermediate state is relatively rarer compared to the other three metropolitan areas. Consequently, the annual MODIS-derived AOD for Beijing was the lowest. We think this would cause an underestimation in the random error of the XCO_2 acquired by CO_2-IPDA LIDAR and that users of the data should be aware of this problem.

Table 3. Environmental parameter statistics obtained from remote sensing products for the four metropolitan areas.

Name		Guangzhou	Wuhan	Shanghai	Beijing
Annual AOD		0.64	0.78	0.95	0.54
annual reflectance		0.168	0.170	0.156	0.190
Area (km^2)		7343	8594	6340	1,6410
Number of observations in 1 month	450 km	838	1625	745	3631
	705 km	142	1232	56	2626
Monthly cloud fraction (%)	Jan.	48.74	66.96	80.73	55.17
	Feb.	83.32	69.21	72.74	50.75
	Mar.	92.33	84.55	75.02	42.04
	Apr.	66.36	71.18	69.78	46.77
	May	92.44	89.08	77.72	45.32
	Jun.	79.23	85.77	89.00	70.77
	Jul.	89.88	75.20	75.38	60.47
	Aug.	76.10	49.3	59.52	56.10
	Sep.	64.50	63.21	69.54	53.55
	Oct.	63.38	42.06	55.26	36.33
	Nov.	73.20	86.60	86.90	87.33
	Dec.	77.92	78.00	84.37	68.23

Figure 6 shows the relative random error of the city-scale XCO_2 values in four metropolitan areas when the orbit height was set as 450 km. Generally, the random error kept below 0.3% for Beijing, Shanghai, and Wuhan. In Guangzhou, only during March and May did the random error slightly exceed 0.3%. Hence, it can be concluded that China's CO_2-IPDA LIDAR could obtain very useful XCO_2 in formation in urban areas if the orbit height was set to 450 km. Moreover, the annual AOD of Guangzhou ranks penultimate amongst the four metropolitan areas. In addition, the reflectance is not evidently lower than in the other metropolitan areas. Hence, we think that the cloud fraction

is a dominant factor when determining the accuracy of the XCO_2 data. Table 3 shows that the cloud fraction was 92.33% and 92.44% in Guangzhou during March and May, respectively. During these two months, the random error exceeded 0.3% in Guangzhou. The accuracy of the XCO_2 data in Beijing was very high; even better than the ideal precision (0.1%). Even though we doubled the annual AOD for Beijing, the random error during most months was still below 0.1%.

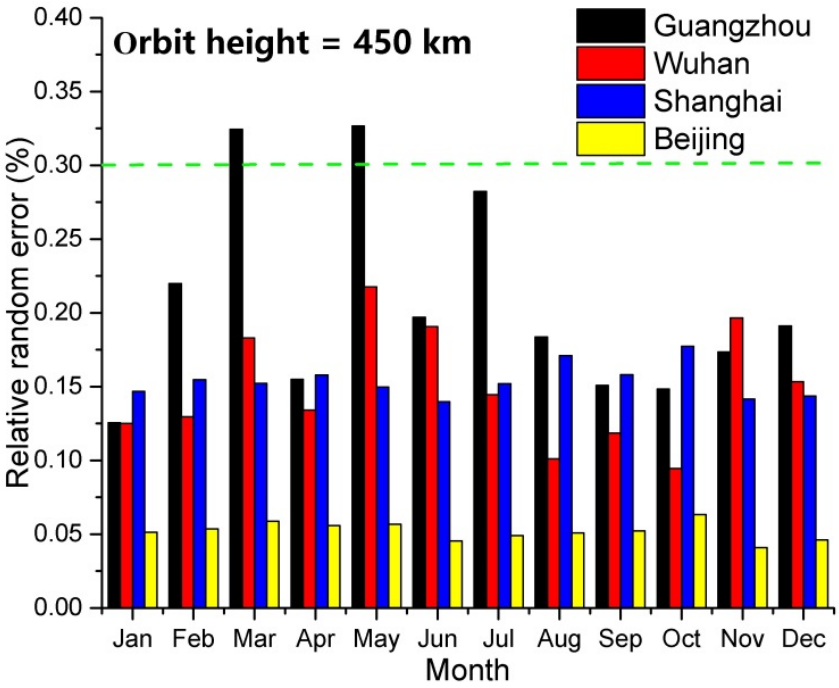

Figure 6. Relative random errors of the city-scale XCO_2 values in different months and metropolitan areas. The orbit height was set as 450 km. The green dotted line marks the target precision of the AEMS initiative.

Figure 7 shows that the relative random error barely stays below 0.3% in Shanghai and Guangzhou regardless of the month when the orbit height was set to 705 km. The relative random error fluctuated around 0.3% in Wuhan. In Beijing, good results are still expected based on the simulations. It is witnessed in Section 3 that the number of observations would be much lower if the orbit height was set to 705 km, in contrast to 450 km. The lack of sufficient observations is a key reason why the performance is so poor when the orbit is set to a higher altitude. Additionally, we can infer from Equations (2) and (3) that the SNR of a single observation would decrease with the increasing detection range (r_G), namely the orbit height. This then would make the accuracy of XCO_2 data even less. With an orbital height of 705 km, it is still possible to obtain precise city-scale XCO_2 measurements in half of the cities. Additionally, we found that the distribution of the nadir sample points were of great significance for determining the random error when the orbit height is 705 km. The importance of the other factors no longer remain evident.

Through these simulations, we also found that a highly accurate single observation is still very challenging. For an orbit height of 705 km, the relative random error of a single observation was 4%, 4.6%, 5.7%, and 3.4% for Guangzhou, Wuhan, Shanghai, and Beijing, respectively. For an orbit height of 450 km, the relative random error was 2.6%, 2.9%, 3.6%, and 2.3% for Guangzhou, Wuhan, Shanghai, and Beijing, respectively. Though those relative random errors significantly exceeded the target precision of 0.3%, the data could still be useful for identifying the carbon source. The target accuracy of 0.3% is defined at a large scale (~50 km). The horizontal gradients of large-scale CO_2 values are very small. This is why the target accuracy for the XCO_2 data acquisition is so high. However, many observations have confirmed that a plant or a mine field can easily cause a horizontal gradient of over

10 ppm (2.5%) [26,55,56]. Hence, we encourage researchers to further investigate the use of a single observation with a random error of 2–4% for the identification or quantification of some anthropogenic emission sources.

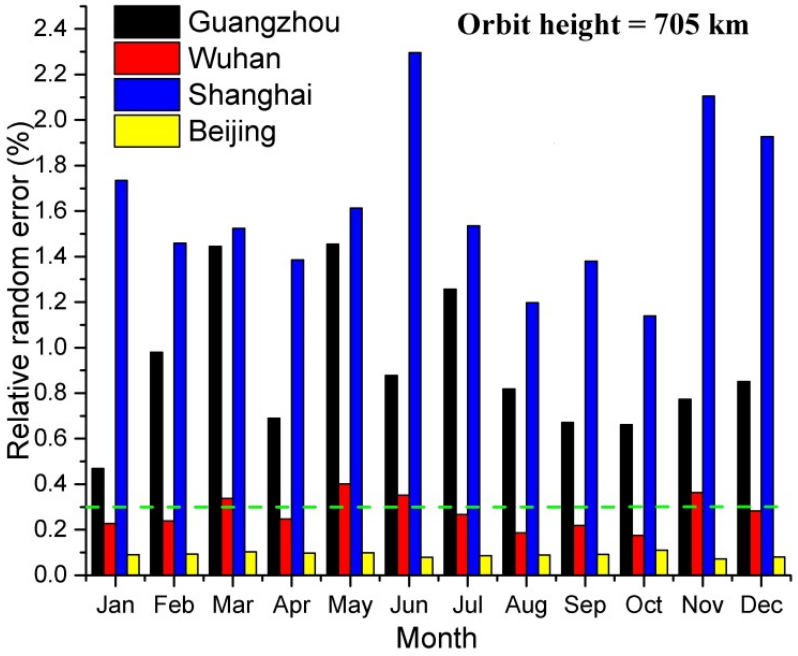

Figure 7. Relative random errors of the city-scale XCO_2 values in different months and metropolitan areas. The orbit height was set as 705 km. A fixed vertical axis scale would be better to compare with the results shown in Figure 8. However, differences between the extents of the vertical axes of the two figures are too large. The green dotted line that marks 0.3% in both figures can help compare the two figures.

3.3. Estimation of the Systematic Error

In our previous study, we briefly demonstrated estimations of the systematic errors [33]. According to that analysis, we found that contributions from uncertainties in the pressure, frequency drift, spectral impurity, and Doppler shift along the track dominate the total systematic error. Hence, we will demonstrate a detailed analysis for these factors. After that, contributions from all factors will be calculated using the methodologies shown in Section 2.4.

Figure 8 shows the relationship between the pressure uncertainty-induced error and the wavenumber. It is worth noting that the pressure uncertainty exerts two types of influences on the retrieval errors. On one hand, the pressure uncertainty would lead to uncertainty in the estimation of the air number density. On the other hand, the pressure uncertainty would lead to uncertainty in the determination of cross-sections. Regarding to the former part, the relevant error was about 0.12 ppm. This part of error is constant with the selection of the on-line wavelength. Additionally, such an error would only emerge when trying to transform the number density of CO_2 to XCO_2. Previous study has already indicated that the number density of CO_2 was useful for calculating the carbon fluxes of strong point emissions [57].

Herein, the so-called pressure uncertainty induced error refers to the latter part because the former part is constant to the wavenumber. The absorption cross-section is calculated by using the Voigt profile which requires the Lorentzian half-width half-maximum (HWHM) as one of the input variables. The Lorentzian HWHM is a function of the pressure [58]. Consequently, the uncertainty of the pressure will propagate to the determination of the Lorentzian HWHM and will eventually propagate to the estimations of the number density for CO_2. As shown in Figure 8, the pressure uncertainty-induced error varied between 0.013–0.035 ppm. For the chosen on-line wavenumber,

that error was 0.017. Compared with the error due to the estimation of the air number density, the pressure uncertainty-induced error is much smaller. Consequently, the total error, geometrical average of two parts, due to the pressure uncertainty would be 0.121 ppm, similar to the results obtained by Ehret et al. [39]. It is worth noting that users should figure out whether they need the number density of CO_2 or XCO_2 to solve their specific problem. If it was reasonable to use the number density of CO_2, the pressure uncertainty-induced error would be a small fraction of the total systematic error.

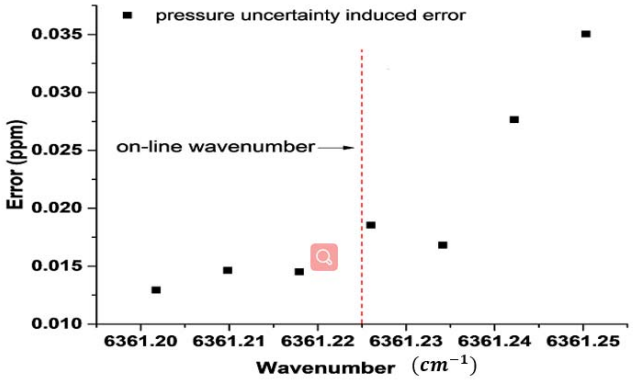

Figure 8. The pressure uncertainty-induced error as a function of wavenumber.

Figure 9 shows the relationship between the frequency drift induced error and the wavenumber. Such an error arises from incorrect calculations of the absorption cross-section that are a function of the wavelength. Actually, frequency drifts of both on-line and off-line wavelengths would bring errors, theoretically. However, the line shape of a Voigt profile is very "smooth" at off-line wavelengths. In addition, the strength of the absorption cross-section at an off-line wavelength is smaller than that at on-line wavelengths by over one order of magnitude. Therefore, we focus on frequency drift of the on-line wavelength herein. The frequency drift induced error reaches its peak at the wings of a CO_2 spectrum, while it falls to a much lower value at the absorption peak according to previous studies [39,59,60]. Consequently the on-line wavenumber could move to the absorption peak of the CO_2 spectrum and the error would decrease by one order of magnitude, as also shown in Figure 9. Such a design would result in an insensitive weighting function for the lower troposphere [33], but a higher differential absorption optical depth (1.1 versus 0.8) resulting in a smaller random error according to Equation (1). For this reason, it is a dilemma when selecting an appropriate on-line wavelength. For the current configuration, the frequency drift induced error would be 0.175 ppm.

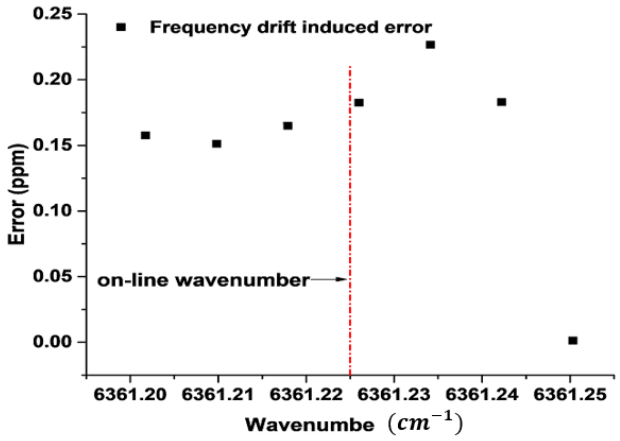

Figure 9. The frequency drift-induced error as a function of wavenumber.

Figure 10 shows the relationship between the spectral impurity-induced error and the wavenumber. Such an error can be divided into two parts related with the detectors and lasers, respectively. On one hand, the filter bandwidth determines the width of the sampling window. Since the width of the signal spectrum is much narrower than that of the background spectrum, a wider sampling window provides a higher possibility of background signals arriving at the detector. On the other hand, the spectral impurity determines the strength of the background signals with respect to the useful signal. Consequently, the perfect solution would be a laser with a low spectral impurity and a detector with a narrow filter bandwidth. Ehret et al. [39] indicated that a spectral impurity of 0.01% with a filter bandwidth of 1 GHz would result in negligible errors. However, Figure 10 shows that the relevant error would be around 0.24 ppm when the spectral impurity is 0.1% and the filter bandwidth is 0.45 nm (~54 GHz). We urge the developers of the CO_2-IPDA LIDAR to significantly improve the spectral purity and the filter bandwidth to reduce the spectral impurity-induced systematic error because such an error dominates the total systematic error.

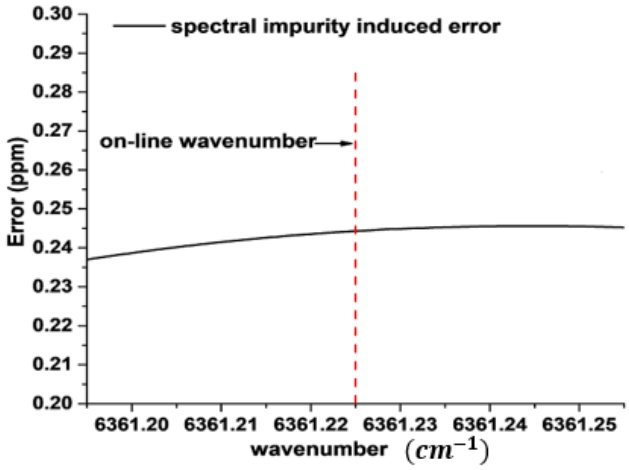

Figure 10. The spectral impurity induced error as a function of wavenumber.

The wind speed is 2–3 orders of magnitude slower than the satellite velocity and the cross-track Doppler shifts are evidently smaller than the along-track Doppler shifts. Thus, we solely discuss errors due to Doppler shifts in this subsection.

Regarding the along-track Doppler shifts, the resultant shifts are 0.53 MHz and 0.54 MHz for orbit heights of 705 km and 450 km, respectively, with the values of the other parameters equal to those shown in Tables 1 and 2. Such shifts would eventually lead to systematic errors of 0.0662% and 0.0674% on the differential absorption optical depth for orbit heights of 705 km and 450 km, respectively, which correspond to 0.265 ppm and 0.270 ppm with a background XCO_2 of 400 ppm. Hence, the error due to the along-track Doppler shifts would be another major systematic error source. Meanwhile, the influence of the orbit height on the along-track Doppler shift induced errors is very small.

4. Discussion

4.1. Potential Uncertainty Due to the AOD Products

There are several environmental factors to be considered in the proposed performance evaluation framework. Though we selected only four representative cities to study the performance of a CO_2-IPDA LIDAR in urban areas, more extensive simulations would be done in the future to achieve detailed results for more cities. This is the reason why we selected remote sensing products as inputs for the environmental factors. However, not all remotely-sensed products are accurate enough. Among these relevant products, the uncertainty in the AOD product is the highest. Hence, there would be inevitable uncertainties in the performance evaluations due to MOIDS-derived AOD products.

Sun photometer-derived AODs from NASAs Aerosol Robotic Network (AERONET) sites are widely used to evaluate the accuracy of MODIS-derived AODs. There are three AERONET sites in Beijing, but none distributed in Shanghai, Guangzhou, or Wuhan. The Taihu Lake site is within 100 km of Shanghai, while the Hong Kong sites are about 130 km away from Guangzhou. Hence, they can be used as proxies for Shanghai and Guangzhou, respectively. Moreover, our group established a Cimel sun photometer CE-318, which is the same equipment used at AERONET sites since 2010. Relationships between sun photometer-derived AODs and MODIS-derived AODs have been established in Beijing [61], Taihu Lake [62], Hong Kong [63], and Wuhan [64], respectively. Through these studies we found that the slopes of the regression equations ranged from 0.8–1.1. The difference between the annual AOD of the two products varied from 0.01–0.34 in terms of the cities. The key factors dominating such a difference were identified as the surface reflectance, AOD, and cloud optical depth [64]. It is very difficult to draw a universal conclusion on whether MODIS-derived AODs overestimate or underestimate the AOD because such differences are highly season- and location-dependent. Consequently, users of the data should be aware of this issue in practical applications.

4.2. Potential of Off-Nadir Modes

The orbit height of the AEMS is designed to be 705 km. Figure 11 presents coverage potential of a 705 km-height orbit with a spiral scan mode. There is little possibility of modifying this parameter at present. Figures 4 and 5 show that gaps between two adjacent tracks are too large to cover important cities with an orbit height of 705 km. Consequently, it is necessary to evaluate the potential of an off-nadir pointing mode to achieve better coverage in urban areas. If the LIDAR could point away from nadir, like NASA's Ice, Cloud, and Land Elevation Satellite/Geoscience Laser Altimeter System (ICESat/GLAS) instrument, better coverage would be expected in any specific metropolitan area of interest. Equation (11) was used in our experiments to simulate the additional coverage brought by spiral scan mode and cross-track scan mode. α is the degree to which the beam can scan away from the nadir, r is the radius of the Earth, β is the angle of curvature corresponding to the maximum coverage, and a is the orbit height. In our simulations α was set to 5°. Equation (11) can, thus, be approximately transformed to Equation (12):

$$tan\alpha = rsin\beta/[a + r(1 - cos\beta)] \quad (11)$$

$$tan\beta = atan\alpha/r \quad (12)$$

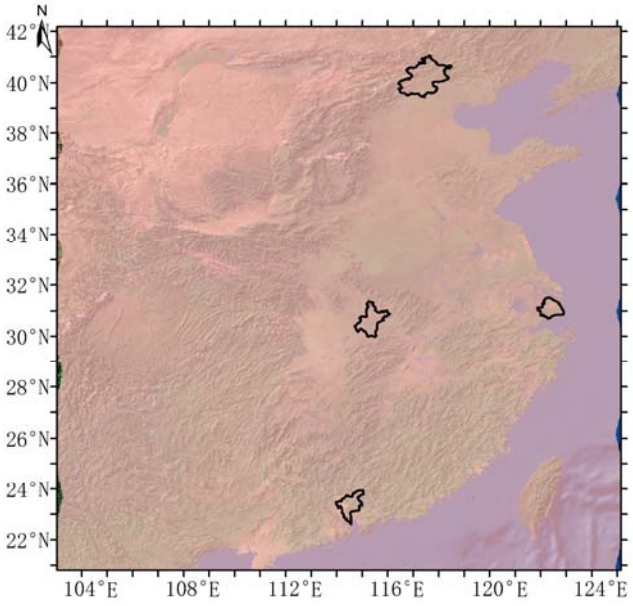

Figure 11. Coverage potential of a 705 km-height orbit with a spiral scan mode.

In Figures 12 and A1, the semitransparent rose areas represent the coverage potential of a 705 km-height orbit with off-nadir modes. It is worth noting that the "coverage potential" never means real coverage. The coverage ability is related to the number of pulses in a certain time period and sampling pattern. Off-nadir modes would only change the sampling patterns, while the number of pulses are determined by the repetition frequency of the laser. Therefore, off-nadir modes cannot amplify coverage areas of the sample points, but can optimize the coverage areas. In other words, we could obtain more sample points in urban areas, but in the meantime we lose an equal number of sample points in other areas. Furthermore, off-nadir modes could lead to additional systematic errors. For the spiral scan mode, additional errors would be inevitable because of the along-track Doppler shifts. For the cross-track scan mode, there would be no additional errors, theoretically. However, additional errors would emerge because the scan plane cannot be strictly perpendicular to the Earth's surface in practical applications. It is also worth noting that any off-nadir mode capabilities would significantly raise the difficulty and the development costs of a CO_2-IPDA LIDAR system.

In the spiral scan mode, the LIDAR was assumed to be able to rotate around the perpendicular direction at a maximum amplitude of 5°. In the cross-track scan mode, the laser can scan perpendicular to the track direction at a maximum amplitude of 5°. Figure A1 shows that there would be no gaps in the spiral scan mode. Figure A1 shows that the gaps would also be very small and even negligible in the cross-track scan mode. With specific programming of the scanning sequence, the coverage of a CO_2-IPDA LIDAR system in metropolitan areas would no longer be a problem. Hence, we recommend that producers of the LIDAR and the satellite platform consider the design of some off-nadir modes. The cross-track scan mode is already adequate for obtaining perfect coverage in urban areas.

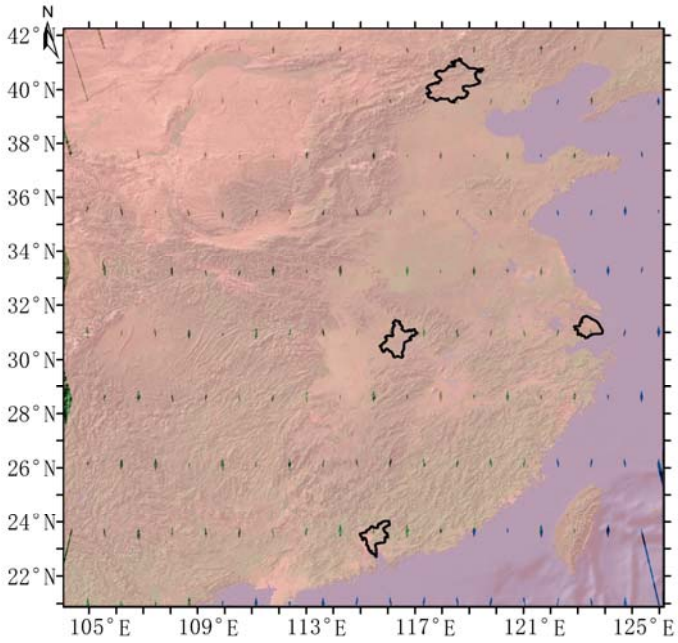

Figure 12. Coverage potential of a 705 km-height orbit with a cross-track scan mode.

4.3. Potential Scientific Applications

As stated in the introduction part, there would be two major scientific applications for satellite-derived XCO_2 products in urban areas, namely estimations of city-scale carbon fluxes and anthropogenic point carbon emissions.

Figures 6 and 7 show that the orbit height of 705 km would hinder a spaceborne CO_2-LIDAR from estimating of city-scale carbon fluxes owing to its resultant heterogeneous distribution of nadir samples. When one tried to retrieve horizontal gradients by using XCO_2 products with such a geographic distribution, the result would be very worrying. In contrast with orbit height of 705 km, an orbit height

of 450 km demonstrates promising ability to obtain homogeneous distribution of samples over urban areas. This feature would be very beneficial for sequent estimation of city-scale fluxes.

Regarding another potential scientific application, namely, estimation of anthropogenic carbon point emission, we did not collect geographic locations of strong point emissions, such as plants and factories in China, at present to perform sophisticated analysis in this work. The reason for that is we cannot simulate exactly where samples are without specification of t_0, as stated in Section 2.5. Some general inferences can still be deduced. An orbit height of 450 km would definitely help us cover more strong points of emissions. However, its longer revisit period may bring trouble in measuring point emissions with variable emission rates. Take cloud cover and heavy pollution into consideration: there might only three useful observations for each point emission per year. According to existing studies on OCO-2, an orbit height of 705 km might cover merely less than 1% of anthropogenic point emissions globally by using the nadir mode. However, for those "lucky" emissions which are located on the nadirs of orbit tracks, there would be more than five useful observations per year in real circumstances.

Regarding the accuracy and the precision, two applications would pose different requirements. Horizontal gradients would be the basis for estimating city-scale carbon fluxes. Then a constant bias in a certain area (e.g., 100 km by 100 km) will not be a problem for this application. Section 3.2 has shown that the random error of a single observation in urban areas varies between 3–6%. If we selected all observations within a radius of 50 km of the target city, there would be 165 background pixels and 110 target pixels to retrieve the CO_2 gradients if the dimension of the target city is 40 km by 40 km (Though the area of Chinese major cities is large, core regions of most major cites do not exceed 40 km by 40 km). Considering that XCO_2 gradients between urban areas and their surroundings are just 3–5 ppm [35], the temporal and spatial resolutions of retrievals must be downscaled to reduce the random error to an acceptable level. Taken 10 km and one year as an example, the random error can be reduced to 0.23–0.46% with a cloud fraction of 0.5. We think the uncertainty of sequent carbon fluxes could be 20–50%, which is an improvement to estimations of city-scale carbon fluxes in developing countries.

Accurate estimation of point carbon emissions relies on unbiased retrievals of XCO_2. The bias of ASEM-CO_2-IPDA would be within 0.2 ppm (see analysis in Section 4.4). This is large in terms of the estimation of continental carbon fluxes. However, a strong point carbon emission can lead to evident elevated XCO_2 (20 ppm or more). Consequently, the overestimation/underestimation of carbon emissions derived from the bias of XCO_2 products acquired by ASEM could be within 1–2%. At present, it is impossible to evaluate the potential uncertainty without specifications of an inversion method for retrieving point carbon emissions by using spaceborne XCO_2 products. However, there would be at least one major advantage over traditional method for any estimation methods using spaceborne XCO_2 products, that is, timeliness. This is very critical for improving the carbon emission exchange trade market. Rapid update to emissions of plants could eventually lead to the emergence of futures markets.

4.4. Further Demands for Improvements of Systematic Errors

From the aspect of random errors, we conclude that it is feasible to precisely measure city-scale XCO_2 values in urban areas where the AOD is higher than other regions, though the precision of single observations is not ideal. Regarding the accuracy of city-scale XCO_2, it was possible to obtain results with a random error less than 0.3% regardless of the city location and season is if we can set the orbit height of the CO_2-IPDA LIDAR system to 450 km. However, if forced to accept an orbit height of 705 km, we could fail to obtain useful measurements in over half of the cities. In this case, we recommend to the designers that they should choose the time at which the satellite passes the ascending node very carefully to cover their priority cities, such as Shanghai and Guangzhou. A better solution would be the introduction of a cross-track scan mode.

According to current configurations, the total systematic error for the given configuration is about 0.51 ppm. The term "systematic errors" in the work follows the definition given by Ehret [39]. It consists of the bias with a non-zero mean and the random systematic error with a zero mean. The significance of systematic errors relies on subsequent applications. For example, if one tried to estimate the carbon emission, bias would bring uncertainties. Oppositely, if one tried to retrieve the CO_2 gradient, a constant bias would be cancelled out through a differential process or a median filter. The bias is mainly owing to the linewidth, the spectral purity, uncertainties of line parameters. The bias derived from the linewidth can be corrected by calibration experiments [65]. Hence, the remaining bias would be around 0.19 ppm. In the assessment report for the A-SCOPE mission, a threshold for the bias was defined as 0.15 ppm. The bias of China's CO_2-IPDA LIDAR system would exceed that threshold. Consequently, it is of great significance to determine the characteristics of bias in laboratory studies before the satellite is launched and to find methods to calibrate the bias.

There is an evident controversy on the uncertainty of meteorological data used in this work because the current weather data assimilation models cannot provide profiles of T and P with uncertainty less than 0.5 k and 0.5 hPa, respectively. The analysis in Section 3.3 has shown that the majority part of errors derived from the uncertainty of meteorological data is actually owing to inaccurate estimation of air density. For the estimation of anthropogenic carbon point emissions, it is not necessary to retrieve the CO_2 concentration in the unit of ppm. The number density is more appropriate for this application. For the estimation of city-scale carbon fluxes, a constant bias is not a problem. Though the error derived from meteorological data is categorized into the systematic error, such an error does not belong to a bias. Uncertainties of profiles of T and P provided by current weather data assimilation models would be 1–2 K and 1–2 hPa, respectively. Therefore, its resultant error would be 0.3–0.6 ppm. Compared with the random error, the meteorological-data-derived error is evidently smaller. However, we should still be very careful with such an error because there is no evidence to prove it is latitude-independent. Consequently, we are looking forward to better weather data assimilation models which are capable of providing meteorological data with the required uncertainty.

Lastly, in this work we have frequently adopted A-SCOPE's threshold for the XCO_2 products. It is worth noting that A-SCOPE's threshold never applies to the estimation of urban carbon fluxes/emissions. A-SCOPE's threshold is just a reference for the performance evaluation of measuring urban XCO_2 using a CO_2-IPDA LIDAR system. A-SCOPE's threshold was derived based on the fact that the horizontal gradient of CO_2 is very small on a continental scale. Oppositely, many studies have shown that XCO_2 surges in urban areas. Hence, the requirement on the precision could be loosened, correspondingly. We urge the carbon cycle community to establish an appropriate standard for estimating urban carbon fluxes/emissions using spaceborne remote sensing of XCO_2 values.

5. Conclusions

To explore the feasibility of precisely measuring XCO_2 values in urban areas using China's planned CO_2-IPDA LIDAR system, a performance evaluation framework that combines a sensor model, a sampling model, and an environmental model was proposed and used to investigate the relative random errors of city-scale XCO_2 measurements. Such a framework comprehensively considered the effect of the hardware, the sampling pattern, as well as the environments. We found that the orbit height plays an extremely significant role in determining whether useful observations can be collected within city boundaries. Subsequently, it was observed that results with random errors of less than 0.3% can be obtained in three out of four cities regardless of the month when the orbit height was set as 450 km. However, when another orbit height, 705 km, was utilized, the results were less reassuring because the random errors significantly exceeded 0.3% in half the cities. It is also worth noting that the random error of less than 0.3% is defined for accurate estimation of carbon fluxes on a continental scale. For XCO_2 measurements in urban areas, its subsequent application should be an estimation of city-scale carbon fluxes or anthropogenic carbon point emissions. Hence, the random error of less than 0.3% is a referential index, but not a compulsory requirement. The simulations also showed

that a cross-track scan mode would solve the insufficient coverage problem. This work confirms the ability of a CO_2-IPDA LIDAR system to accurately measure city-scale XCO_2 in high AOD conditions. Additionally, we found that the cloud fraction is also an important factor for increasing the precision. Considering that the cloud fraction used in this work was provided by a MODIS product, the smaller footprint of an IPDA would definitely lead to a smaller cloud fraction because blanks or holes in the clouds would permit useful laser measurements. Moreover, lasers can penetrate some of the optically thin clouds. Consequently, better performances would be expected under real conditions. Another critical issue is to develop methods for estimating city-scale carbon fluxes or anthropogenic carbon point emission by means of satellite-based remotely-sensed XCO_2 data. Only in that case, we would know clearly the ability of those novel sensors to help us solve some key problems in carbon cycle studies.

Author Contributions: G.H. proposed the idea and wrote the manuscript. X.M. corrected the manuscript and collected necessary data and parameters. J.L. and J.D. provided information on CO_2-IPDA LIDAR. H.X. and A.L. conducted the experiments. W.G. funded this research and negotiated with the cooperators mentioned in the acknowledgments.

Funding: This work was supported by the National Key R and D Program of China (grant no. 2017YFC0212600), the National Natural Science Foundation of China (grant nos. 41601351, 41627804 and 41127901), and a China Postdoctoral Science Foundation funded project (grant no. 2017T100580).

Acknowledgments: The authors wish to thank Qing Li and Pengfei Ma at the Satellite Environment Center, Ministry of Environmental Protection, Fu Wang at National Satellite Meteorological Center, China Meteorological Administration, and Weibiao Chen at the Shanghai Institute of Optics and Fine Mechanics, and the Chinese Academy of Sciences for providing the configuration of the CO2-IPDA LIDAR and information on the AEMS. The authors also thank Yannan Zhao, with the Key Laboratory of Earthquake Geodesy, Institute of Seismology, China Earthquake Administration, for her skillful analysis and graphics.

Conflicts of Interest: The authors declare no conflict of interest.

Appendix A. Introduction to ASEM-CO_2-IPDA

The focus of this work is performance evaluation of the CO_2-IPDA LIDAR. Its configuration is shown in Table A1.

Table A1. The parameter configuration of China's CO_2-IPDA.

Category	Parameter Name	Value	Unit
Laser transmitter	Pulse length	15	ns
	On-line wavelength	6361.225	cm^{-1}
	Off-line wavelength	6360.981	cm^{-1}
	Fluctuation of pulse energy	1	%
	Fluctuation of ratio of on-line and off-line pulse energy	0.1	%
	Linewidth	50	MHz
	Stability of on-line wavelength	0.6	MHz
	Spectral purity	99.9	%
	Energy per pulse	75	mJ
	Repetition frequency (a pair of on-line and off-line)	20	Hz
	Interval time between successive beams	200	us
	Divergence angle	100	urad
Telescope	Time interval of contiguous pair	0.2	ms
	Diameter	1	m
	Overall optical efficiency	51.8	%
	Optical filter bandwidth	0.45	nm
Other	Field of view	0.2	mrad
	Electronic bandwidth	3	MHz
	Dark current (noise equivalent power)	64	$fW/\sqrt{Hz}$
	Quantum efficiency	73	%
	Internal gain	9	
	Excess noise factor	3.2	
	Orbit altitude	705	km
	Orbit type	1 h/13 h sun-synchronous	
	Viewing geometry	Nadir	

The load-related parameters are consistent with that of China's CO_2-IPDA LIDAR, which is under development at the Shanghai Institute of Optics and Fine Mechanics, at the Chinese Academy of Sciences. It is worth noting that values of parameters presented in Han G et al. [33] are the requirements of the CO_2-IPDA LIDAR. The recent development of that sensor is described in Du J et al. [47].

Figure A1 shows the schematic diagram of the CO_2-IPDA LIDAR. It includes three parts: a laser transmitter subsystem, a receiver subsystem, and a data acquisition system. The transmitter subsystem consists of a 1572 nm double pulsed laser, a pulse energy monitoring unit, and a pulse frequency monitoring unit. In the receiver subsystem, there is a Schmidt–Cassegrain telescope and a Licel InGaAs avalanche photodiode (APD) module for CO_2 detection. The data acquisition unit is based on two 14-bit, 100 MS/s digitizers (NI PCI5122). Digitizers and data storage were hosted by means of a personal computer. It is worth noting that this is just a prototype of the CO_2-IPDA. It is expected that certain modifications and improvements will be applied in the future.

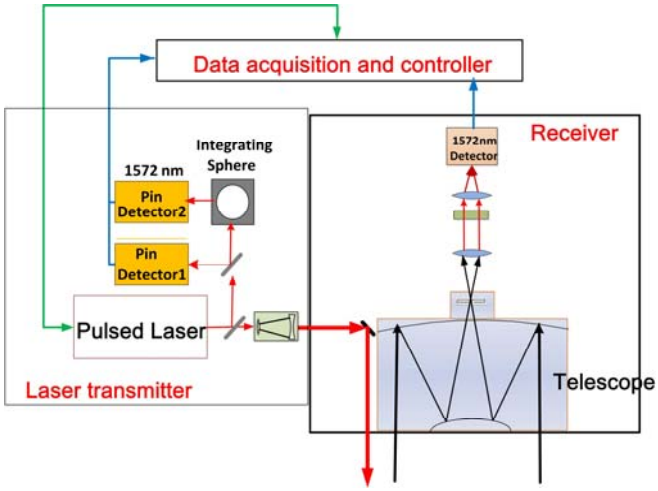

Figure A1. Schematic diagram of the CO2-IPDA LIDAR.

The transmitter subsystem consisted of a pulsed laser, a pulse energy monitoring unit, and a pulse frequency monitoring unit. The frequency-stabilized 1572 nm pulsed laser was obtained through a seeder-injected optical parametric oscillator (OPO). Special features included a frequency stabilized seeder laser providing alternating two narrow band wavelengths around 1.572 μm and a highly-stabilized OPO with the single-pass ring configuration. The seeder laser actually contained three distributed-feedback (DFB) laser diodes: one served as a reference laser (RL) that was wavelength locked to a CO_2 line center at 1572.0179 nm using the external frequency modulation technique, and the other two acted as online-seeder and offline-seeder lasers that were offset locked to the RL at 1572.024 nm and 1572.084 nm, respectively, based on optical phase-locked loop technology. The OPO system served as a tunable frequency converter to obtain the desired wavelengths. Figure 3 shows the schematic of the OPO. The injection-seeded, electro-optical Q-switched, and laser diode (LD)-pumped Nd:YAG laser acted as the pump radiation for the OPO [19]. The OPO was designed as a single-pass ring configuration to avoid back reflections damaging the seeder laser or resulting in spectral instabilities. KTP crystal acted as a non-linear medium and worked in the type II non-critically phase-matched mode. The OPO cavity was matched to the seeder-laser by a resonance detection technique through a piezoelectric ceramic transducer (PZT) element to control the cavity length.

In the pulse energy monitoring unit, part of the 1572 nm transmitting laser was sampled by an integrating sphere and received by an InGaAs positive-intrinsic negative (PIN) detector (Thorlabs PDA20CS). The detector offered a switchable gain and bandwidth with low noise-equivalent-power (NEP).

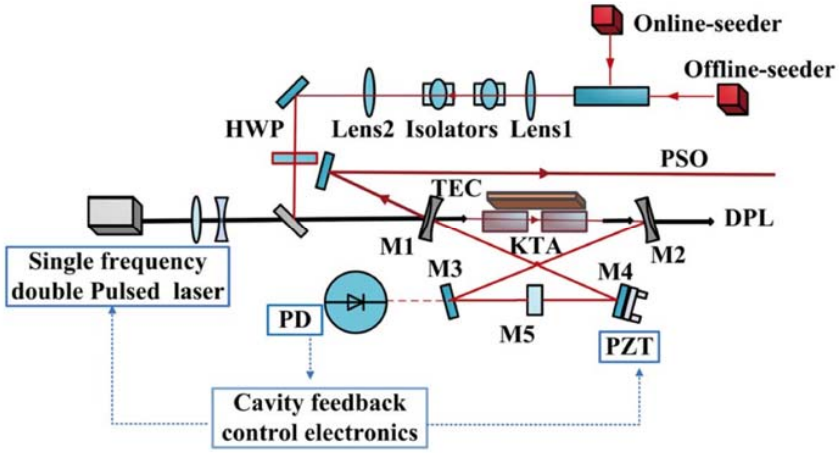

Figure A2. Schematic diagram of OPO for the LIDAR transmitter. HWP, half wavelength plate; DPL, depleted pump laser; PSO, pulsed signal output; PD, photo detector; TEC, thermoelectric cooler; BS, beam splitter; and OS, optical switch.

Appendix B. Description of Calculation Method of the Random Error

In the main body we have already described briefly how to calculate the random error. In this appendix we demonstrate detailed information on how to further calculate SNR. $SNR_{on,off}$ can be then expressed as follows [39]:

$$SNR_{on,off} = \frac{P_{on,off} MR}{B\left(2eM^2FR\left(P_{on,off} + P_{back}\right) + i_D^2\right)} \tag{A1}$$

where M is the detector internal gain factor, R denotes the detector's responsivity, B is the electrical bandwidth, e is the elementary charge, F is the detector's excess noise factor, which accounts for additional noise due to the internal amplification statistics, and i_D^2 is the dark current noise density. In simulations of this work, values of the above variables are consistent with Table A1 (detector part). P_{back} is the power of solar background radiance and can be calculated as follows:

$$P_{back} = \frac{FOV^2 A^2 LQ}{4}. \tag{A2}$$

where Q is the reflectance of the target and A is the effective detection area of the telescope. FOV is the field of view of the detection system. L is the solar radiance. Our previous study demonstrated that, with the current configuration of the LIDAR system, even with the solar radiance amplified 10 times its normal value the resultant random errors were still negligible [33]. In this work, L is set to be 10 mW/(m^2·nm·sr). $P_{on,off}$ can be expressed as follows [39]:

$$P_{on,off}(r_G) = D_{on,off} \frac{A}{r_G^2} O_{on,off} \frac{Q_{on,off}}{\pi} \tau_{on,off}^2 \frac{E_{on,off}}{\Delta t_{eff}}. \tag{A3}$$

$$\Delta t_{eff} = \sqrt{\Delta {\tau_L}^2 + \left(\frac{1}{3B}\right)^2 + \left(\frac{2\Delta h}{c}\right)^2} \tag{A4}$$

$$\tau = e^{\left(-AOD - \int_{P_{surface}}^{P_{toa}} N_{CO_2}(p)\sigma_{CO_2}(\lambda,p) + N_{H_2O}(p)\sigma_{H_2O}(\lambda,p)dp\right)} \tag{A5}$$

where D is the total optical efficiency of the CO_2-IPDA LIDAR, O is the overlap function, r_G is the detection range, and E is the pulse energy of the transmitted laser radiation. $\Delta teff$ is introduced to account for the effective pulse length of the LIDAR returns and is calculated by Equation (A4).

In Equation (A4), $\Delta\tau_L$ is the pulse length, Δh is the effective target altitude within the footprint of the laser pulse, c is the speed of light, r_G is distance between the target and the laser, and τ is the one-way atmospheric transmission, which can be calculated by Equation (A5). AOD is the aerosol optical depth. N is the number density. σ is absorption cross-section which can be determined by the Voigt profile. Relevant line parameters are according to HITRAN 2016 [66]. A further description of relevant parameters, such as molecular spectra, laser line shape, etc., and the equation of the Voigt profile can be found in references on laser spectroscopy [39,41,58,67].

It is worth noting that an optical filter with an extreme narrow bandwidth is required to minimize the solar background. Narrow optical filters do not have transmission peaks that are perfectly flat, hence, there is at least a small difference in values of D for the on- and off-line wavelengths. Moreover, the output energy of different wavelengths would be set as unequal purposely with a given total output power to reduce the random error [68]. Therefore, it is of great importance to precisely monitor the ratio of on-line and off-line pulse energy.

Figure A3 shows the importance of these parameters and the method employed to estimate the random errors using the equations shown above.

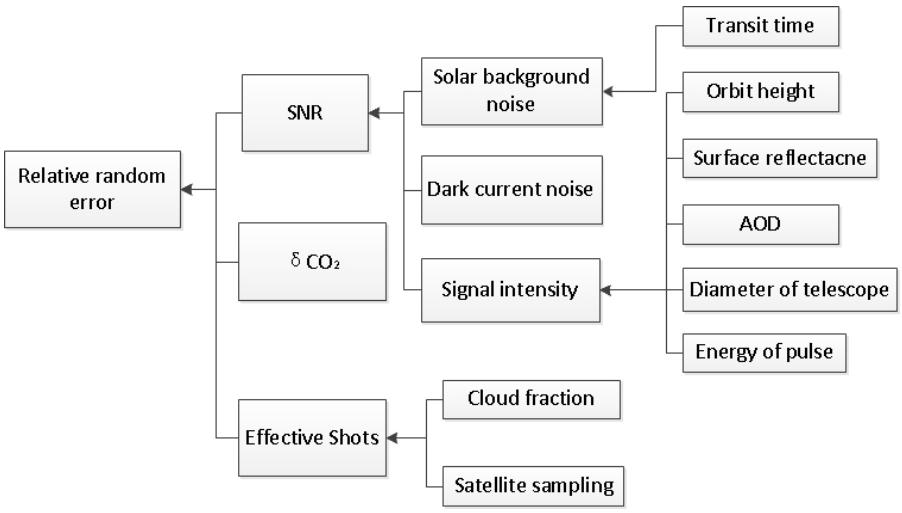

Figure A3. Schematic diagram for the estimation of random errors.

References

1. Stocker, T.F.; Qin, D.; Plattner, G.-K.; Tignor, M.; Allen, S.K.; Boschung, J.; Nauels, A.; Xia, Y.; Bex, V.; Midgley, P.M. IPCC, 2013: Climate change 2013: The physical science basis. In *Contribution of Working Group I to the Fifth Assessment Report of the Intergovernmental Panel on Climate Change*; Cambridge University Press: Cambridge, UK; New York, NY, USA, 2013.
2. Liu, L.; Chen, C.; Zhao, Y.; Zhao, E. China's carbon-emissions trading: Overview, challenges and future. *Renew. Sustain. Energy Rev.* **2015**, *49*, 254–266. [CrossRef]
3. Birol, F. *World Energy Outlook 2010*; International Energy Agency: Paris, France, 2010.
4. Sellers, P.; Dickinson, R.; Randall, D.; Betts, A.; Hall, F.; Berry, J.; Collatz, G.; Denning, A.; Mooney, H.; Nobre, C. Modeling the exchanges of energy, water, and carbon between continents and the atmosphere. *Science* **1997**, *275*, 502–509. [CrossRef] [PubMed]
5. Normile, D. Round and round a guide to the carbon cycle. *Science* **2009**, *325*, 1642–1643. [CrossRef] [PubMed]
6. Gurney, K.R.; Law, R.M.; Denning, A.S.; Rayner, P.J.; Baker, D.; Bousquet, P.; Bruhwiler, L.; Chen, Y.H.; Ciais, P.; Fan, S.; et al. Towards robust regional estimates of CO_2 sources and sinks using atmospheric transport models. *Nature* **2002**, *415*, 626–630. [CrossRef] [PubMed]
7. Rayner, P.; O'Brien, D. The utility of remotely sensed CO_2 concentration data in surface source inversions. *Geophys. Res. Lett.* **2001**, *28*, 175–178. [CrossRef]

8. Paris, J.D.; Ciais, P.; Nédélec, P.; Ramonet, M.; Belan, B.; Arshinov, M.; Golitsyn, G.; Granberg, I.; Stohl, A.; Cayez, G. The YAK-AEROSIB transcontinental aircraft campaigns: New insights on the transport of CO_2, CO and O_3 across siberia. *Tellus B* **2008**, *60*, 551–568. [CrossRef]
9. Lin, J.; Gerbig, C.; Wofsy, S.; Daube, B.; Matross, D.; Chow, V.; Gottlieb, E.; Andrews, A.; Pathmathevan, M.; Munger, J. What have we learned from intensive atmospheric sampling field programmes of CO_2? *Tellus B* **2006**, *58*, 331–343. [CrossRef]
10. LAI, C.T.; Schauer, A.J.; Owensby, C.; Ham, J.M.; Helliker, B.; Tans, P.P.; Ehleringer, J.R. Regional CO_2 fluxes inferred from mixing ratio measurements: Estimates from flask air samples in central Kansas, USA. *Tellus B* **2006**, *58*, 523–536. [CrossRef]
11. McKain, K.; Wofsy, S.C.; Nehrkorn, T.; Eluszkiewicz, J.; Ehleringer, J.R.; Stephens, B.B. Assessment of ground-based atmospheric observations for verification of greenhouse gas emissions from an urban region. *Proc. Natl. Acad. Sci. USA* **2012**, *109*, 8423–8428. [CrossRef] [PubMed]
12. Chevallier, F.; Maksyutov, S.; Bousquet, P.; Bréon, F.M.; Saito, R.; Yoshida, Y.; Yokota, T. On the accuracy of the CO_2 surface fluxes to be estimated from the gosat observations. *Geophys. Res. Lett.* **2009**, *36*. [CrossRef]
13. Liu, Y.; Yang, D.; Cai, Z. A retrieval algorithm for tansat XCO_2 observation: Retrieval experiments using gosat data. *Chin. Sci. Bull.* **2013**, *58*, 1520–1523. [CrossRef]
14. Miller, J.B.; Tans, P.P.; Gloor, M. Steps for success of OCO-2. *Nat. Geosci.* **2014**, *7*, 691. [CrossRef]
15. Crisp, D.; Bösch, H.; Brown, L.; Castano, R.; Christi, M.; Connor, B.; Frankenberg, C.; McDuffie, J.; Miller, C.; Natraj, V. OCO (Orbiting Carbon Observatory)-2 Level 2 Full Physics Retrieval Algorithm Theoretical Basis. 2010. Available online: http://disc.sci.gsfc.nasa.gov/acdisc/documentation/OCO-2_L2_FP_ATBDv1_rev4_Nov10.pdf (accessed on 19 June 2018).
16. Connor, B.; Bosch, H.; McDuffie, J.; Taylor, T.; Fu, D.J.; Frankenberg, C.; O'Dell, C.; Payne, V.H.; Gunson, M.; Pollock, R.; et al. Quantification of uncertainties in OCO-2 measurements of XCO_2: Simulations and linear error analysis. *Atmos. Meas. Tech.* **2016**, *9*, 5227–5238. [CrossRef]
17. Houweling, S.; Hartmann, W.; Aben, I.; Schrijver, H.; Skidmore, J.; Roelofs, G.-J.; Breon, F.-M. Evidence of systematic errors in sciamachy-observed CO_2 due to aerosols. *Atmos. Chem. Phys.* **2005**, *5*, 3003–3013. [CrossRef]
18. Liang, A.; Han, G.; Gong, W.; Yang, J.; Xiang, C. Comparison of global XCO_2 concentrations from OCO-2 with tccon data in terms of latitude zones. *IEEE J. Sel. Top. Appl. Earth Obs. Remote Sens.* **2017**, *10*, 2491–2498. [CrossRef]
19. Liang, A.L.; Gong, W.; Han, G.; Xiang, C.Z. Comparison of satellite-observed XCO_2 from gosat, OCO-2, and ground-based tccon. *Remote Sens.* **2017**, *9*, 1033. [CrossRef]
20. Menzies, R.T.; Tratt, D.M. Differential laser absorption spectrometry for global profiling of tropospheric carbon dioxide: Selection of optimum sounding frequencies for high-precision measurements. *Appl. Opt.* **2003**, *42*, 6569–6577. [CrossRef] [PubMed]
21. Han, G.; Cui, X.; Liang, A.; Ma, X.; Zhang, T.; Gong, W. A CO_2 profile retrieving method based on chebyshev fitting for ground-based dial. *IEEE Trans. Geosci. Remote Sens.* **2017**, *55*, 6099–6110. [CrossRef]
22. Abshire, J.B.; Ramanathan, A.; Riris, H.; Mao, J.P.; Allan, G.R.; Hasselbrack, W.E.; Weaver, C.J.; Browell, E.V. Airborne measurements of CO_2 column concentration and range using a pulsed direct- detection ipda LIDAR. *Remote Sens.* **2014**, *6*, 443–469. [CrossRef]
23. Lin, B.; Nehrir, A.R.; Harrison, F.W.; Browell, E.V.; Ismail, S.; Obland, M.D.; Campbell, J.; Dobler, J.; Meadows, B.; Fan, T.-F.; et al. Atmospheric CO_2 column measurements in cloudy conditions using intensity-modulated continuous-wave LIDAR at 1.57 micron. *Opt. Express* **2015**, *23*, A582–A593. [CrossRef] [PubMed]
24. Refaat, T.F.; Singh, U.N.; Yu, J.; Petros, M.; Ismail, S.; Kavaya, M.J.; Davis, K.J. Evaluation of an airborne triple-pulsed 2 μm ipda LIDAR for simultaneous and independent atmospheric water vapor and carbon dioxide measurements. *Appl. Opt.* **2015**, *54*, 1387–1398. [CrossRef] [PubMed]
25. Yu, J.; Petros, M.; Singh, U.N.; Refaat, T.F.; Reithmaier, K.; Remus, R.G.; Johnson, W. An airborne 2-μm double-pulsed direct-detection LIDAR instrument for atmospheric CO_2 column measurements. *J. Atmos. Ocean. Technol.* **2017**, *34*, 385–400. [CrossRef]
26. Amediek, A.; Ehret, G.; Fix, A.; Wirth, M.; Budenbender, C.; Quatrevalet, M.; Kiemle, C.; Gerbig, C. CHARM-F—A new airborne integrated-path differential-absorption LIDAR for carbon dioxide and methane observations: Measurement performance and quantification of strong point source emissions. *Appl. Opt.* **2017**, *56*, 5182–5197. [CrossRef] [PubMed]

27. Amediek, A.; Fix, A.; Wirth, M.; Ehret, G. Development of an opo system at 1.57 µm for integrated path dial measurement of atmospheric carbon dioxide. *Appl. Phys. B* **2008**, *92*, 295–302. [CrossRef]
28. Amediek, A.; Sun, X.L.; Abshire, J.B. Analysis of range measurements from a pulsed airborne CO_2 integrated path differential absorption LIDAR. *IEEE Trans. Geosci. Remote Sens.* **2013**, *51*, 2498–2504. [CrossRef]
29. Dobler, J.; Braun, M.; Blume, N.; Zaccheo, T.S. A new laser based approach for measuring atmospheric greenhouse gases. *Remote Sens.* **2013**, *5*, 6284–6304. [CrossRef]
30. Menzies, R.T.; Spiers, G.D.; Jacob, J. Airborne laser absorption spectrometer measurements of atmospheric CO_2 column mole fractions: Source and sink detection and environmental impacts on retrievals. *J. Atmos. Ocean. Technol.* **2014**, *31*, 404–421. [CrossRef]
31. Kameyama, S.; Imaki, M.; Hirano, Y.; Ueno, S.; Kawakami, S.; Sakaizawa, D.; Kimura, T.; Nakajima, M. Feasibility study on 1.6 µm continuous-wave modulation laser absorption spectrometer system for measurement of global CO_2 concentration from a satellite. *Appl. Opt.* **2011**, *50*, 2055–2068. [CrossRef] [PubMed]
32. Sakaizawa, D.; Kawakami, S.; Nakajima, M.; Sawa, Y.; Matsueda, H.; Asai, K.; Kameyama, S.; Imaki, M.; Hirano, Y.; Ueno, S. Path-averaged atmospheric CO2 measurement using a 1.57 µm active remote sensor compared with multi-positioned in situ sensors. *Proc. SPIE* **2009**. [CrossRef]
33. Han, G.; Ma, X.; Liang, A.; Zhang, T.; Zhao, Y.; Zhang, M.; Gong, W. Performance evaluation for China's planned CO_2-ipda. *Remote Sens.* **2017**, *9*, 768. [CrossRef]
34. Ingmann, P.; Bensi, P.; Durand, Y. A-scope-advanced space carbon and climate observation of planet erath. In *ESA Report for Assessment, SP-1313/1*; ESA Communication Production Office: Noordwijk, The Netherlands, 2008.
35. Hakkarainen, J.; Ialongo, I.; Tamminen, J. Direct space-based observations of anthropogenic CO_2 emission areas from OCO-2. *Geophys. Res. Lett.* **2016**, *43*. [CrossRef]
36. Kiemle, C.; Ehret, G.; Amediek, A.; Fix, A.; Quatrevalet, M.; Wirth, M. Potential of spaceborne LIDAR measurements of carbon dioxide and methane emissions from strong point sources. *Remote Sens.* **2017**, *9*, 1137. [CrossRef]
37. Bousquet, P.; Peylin, P.; Ciais, P.; Ramonet, M.; Monfray, P. Inverse modeling of annual atmospheric CO_2 sources and sinks: 2. Sensitivity study. *J. Geophys. Res. Atmos.* **1999**, *104*, 26179–26193. [CrossRef]
38. Bousquet, P.; Ciais, P.; Peylin, P.; Ramonet, M.; Monfray, P. Inverse modeling of annual atmospheric CO_2 sources and sinks: 1. Method and control inversion. *J. Geophys. Res. Atmos.* **1999**, *104*, 26161–26178. [CrossRef]
39. Ehret, G.; Kiemle, C.; Wirth, M.; Amediek, A.; Fix, A.; Houweling, S. Space-borne remote sensing of CO_2, CH4, and N_2O by integrated path differential absorption LIDAR: A sensitivity analysis. *Appl. Phys. B* **2008**, *90*, 593–608. [CrossRef]
40. Kawa, S.; Mao, J.; Abshire, J.; Collatz, G.; Sun, X.; Weaver, C. Simulation studies for a space-based CO_2 LIDAR mission. *Tellus B* **2010**, *62*, 759–769. [CrossRef]
41. Kiemle, C.; Kawa, S.R.; Quatrevalet, M.; Browell, E.V. Performance simulations for a spaceborne methane LIDAR mission. *J. Geophys. Res. Atmos.* **2014**, *119*, 4365–4379. [CrossRef]
42. Mao, J.; Ramanathan, A.; Abshire, J.B.; Kawa, S.R.; Riris, H.; Allan, G.R.; Rodriguez, M.; Hasselbrack, W.E.; Sun, X.; Numata, K. Measurement of atmospheric CO_2 column concentrations to cloud tops with a pulsed multi-wavelength airborne LIDAR. *Atmos. Meas. Tech.* **2018**, *11*, 1–26. [CrossRef]
43. Ramanathan, A.K.; Mao, J.P.; Abshire, J.B.; Allan, G.R. Remote sensing measurements of the CO_2 mixing ratio in the planetary boundary layer using cloud slicing with airborne LIDAR. *Geophys. Res. Lett.* **2015**, *42*, 2055–2062. [CrossRef]
44. Kiemle, C.; Quatrevalet, M.; Ehret, G.; Amediek, A.; Fix, A.; Wirth, M. Sensitivity studies for a space-based methane LIDAR mission. *Atmos. Meas. Tech.* **2011**, *4*, 2195–2211. [CrossRef]
45. Predoi-Cross, A.; McKella, A.R.W.; Chiris Benner, D.; Devi, M.V.; Gamache, R.R.; Miller, C.E.; Toth, R.A.; Brown, L.R. Temperature dependences for air-broadened lorentz half-width and pressure shift coefficients in the 30013←00001 and 30012←00001 bands of CO_2 near 1600 nm. *Can. J. Phys.* **2009**, *87*, 517–535. [CrossRef]
46. Rothman, L.S.; Gordon, I.E.; Babikov, Y.; Barbe, A.; Chris Benner, D.; Bernath, P.F.; Birk, M.; Bizzocchi, L.; Boudon, V.; Brown, L.R.; et al. The hitran2012 molecular spectroscopic database. *J. Quant. Spectrosc. Radiat. Transf.* **2013**, *130*, 4–50. [CrossRef]
47. Du, J.; Zhu, Y.D.; Li, S.G.; Zhang, J.X.; Sun, Y.G.; Zang, H.G.; Liu, D.; Ma, X.H.; Bi, D.C.; Liu, J.Q.; et al. Double-pulse 1.57 mu m integrated path differential absorption LIDAR ground validation for atmospheric carbon dioxide measurement. *Appl. Opt.* **2017**, *56*, 7053–7058. [CrossRef] [PubMed]

48. Singh, U.N.; Refaat, T.F.; Ismail, S.; Davis, K.J.; Kawa, S.R.; Menzies, R.T.; Petros, M. Feasibility study of a space-based high pulse energy 2 μm CO_2 ipda LIDAR. *Appl. Opt.* **2017**, *56*, 6531–6547. [CrossRef] [PubMed]
49. Amediek, A.; Fix, A.; Ehret, G.; Caron, J.; Durand, Y. Airborne LIDAR reflectance measurements at 1.57 mu m in support of the a-scope mission for atmospheric CO_2. *Atmos. Meas. Tech.* **2009**, *2*, 755–772. [CrossRef]
50. Disney, M.I.; Lewis, P.E.; Bouvet, M.; Prieto-Blanco, A.; Hancock, S. Quantifying surface reflectivity for spaceborne LIDAR via two independent methods. *IEEE Trans. Geosci. Remote Sens.* **2009**, *47*, 3262–3271. [CrossRef]
51. Han, G.; Gong, W.; Quan, J.; Li, J.; Zhang, M. Study on spatial and temporal distributions of contaminants emitted by chinese new year'eve celebrations in wuhan. *Environ. Sci. Process. Impacts* **2014**, *16*, 916–923. [CrossRef] [PubMed]
52. Hutchison, K.D.; Smith, S.; Faruqui, S. The use of MODIS data and aerosol products for air quality prediction. *Atmos. Environ.* **2004**, *38*, 5057–5070. [CrossRef]
53. Gupta, P.; Christopher, S.A.; Wang, J.; Gehrig, R.; Lee, Y.; Kumar, N. Satellite remote sensing of particulate matter and air quality assessment over global cities. *Atmos. Environ.* **2006**, *40*, 5880–5892. [CrossRef]
54. Cyranoski, D. Satellite view alerts china to soaring pollution. *Nature* **2005**, *437*, 12. [CrossRef] [PubMed]
55. Bovensmann, H.; Buchwitz, M.; Burrows, J.P.; Reuter, M.; Krings, T.; Gerilowski, K.; Schneising, O.; Heymann, J.; Tretner, A.; Erzinger, J. A remote sensing technique for global monitoring of power plant CO_2 emissions from space and related applications. *Atmos. Meas. Tech.* **2010**, *3*, 781–811. [CrossRef]
56. Kotthaus, S.; Grimmond, C.S.B. Identification of micro-scale anthropogenic CO_2, heat and moisture sources—processing eddy covariance fluxes for a dense urban environment. *Atmos. Environ.* **2012**, *57*, 301–316. [CrossRef]
57. Aiuppa, A.; Fiorani, L.; Santoro, S.; Parracino, S.; Nuvoli, M.; Chiodini, G.; Minopoli, C.; Tamburello, G. New ground-based LIDAR enables volcanic CO_2 flux measurements. *Sci. Rep.* **2015**, *5*, 13614. [CrossRef] [PubMed]
58. Han, G.; Gong, W.; Lin, H.; Ma, X.; Xiang, Z. Study on influences of atmospheric factors on vertical profile retrieving from ground-based dial at 1.6 μm. *IEEE Trans. Geosci. Remote Sens.* **2015**, *53*, 3221–3234. [CrossRef]
59. Han, G.; Gong, W.; Lin, H.; Ma, X.; Xiang, C. On-line wavelength calibration of pulsed laser for CO_2 dial sensing. *Appl. Phys. B* **2014**, *117*, 1041–1053. [CrossRef]
60. Koch, G.J.; Beyon, J.Y.; Gibert, F.; Barnes, B.W.; Ismail, S.; Petros, M.; Petzar, P.J.; Yu, J.; Modlin, E.A.; Davis, K.J. Side-line tunable laser transmitter for differential absorption LIDAR measurements of CO_2: Design and application to atmospheric measurements. *Appl. Opt.* **2008**, *47*, 944–956. [CrossRef] [PubMed]
61. Nichol, J.; Bilal, M. Validation of MODIS 3 km resolution aerosol optical depth retrievals over asia. *Remote Sens.* **2016**, *8*, 328. [CrossRef]
62. He, Q.; Li, C.; Tang, X.; Li, H.; Geng, F.; Wu, Y. Validation of MODIS derived aerosol optical depth over the yangtze river delta in china. *Remote Sens. Environ.* **2012**, *114*, 1649–1661. [CrossRef]
63. Man, S.W.; Shahzad, M.; Nichol, J.; Chan, P.W.; Chan, P.W. Validation of MODIS, misr, omi, and calipso aerosol optical thickness using ground-based sunphotometers in Hong Kong. *Int. J. Remote Sens.* **2013**, *34*, 897–918.
64. Wang, W.; Mao, F.; Pan, Z.; Du, L.; Gong, W. Validation of viirs aod through a comparison with a sun photometer and MODIS aods over Wuhan. *Remote Sens.* **2017**, *9*, 403. [CrossRef]
65. Han, G.; Gong, W.; Ma, X.; Xiang, C.; Liang, A.; Zheng, Y. A ground-based differential absorption LIDAR for atmospheric vertical CO_2 profiling. *Acta Phys. Sin.* **2015**, *64*, 244206.
66. Hill, C.; Gordon, I.E.; Kochanov, R.V.; Barrett, L.; Wilzewski, J.S.; Rothman, L.S. Hitranonline: An online interface and the flexible representation of spectroscopic data in the hitran database. *J. Quant. Spectrosc. Radiat. Transf.* **2016**, *177*, 4–14. [CrossRef]
67. Han, G.; Xu, H.; Gong, W.; Ma, X.; Liang, A. Simulations of a multi-wavelength differential absorption LIDAR method for CO_2 measurement. *Appl. Opt.* **2017**, *56*, 8532–8540. [CrossRef] [PubMed]
68. Caron, J.; Durand, Y. Operating wavelengths optimization for a spaceborne LIDAR measuring atmospheric CO_2. *Appl. Opt.* **2009**, *48*, 5413–5422. [CrossRef] [PubMed]